Supplemental material for

"Towards On-Demand Heralded Single-Photon Sources via Photon Blockade"

Jiangshan Tang,[1,2] Lei Tang,[1] Haodong Wu,[1] Yang Wu,[1,3] Hui Sun,[3*] Han Zhang,[1,2†]
Tao Li,[4] Yanqing Lu （陆延青）,[1,2] Min Xiao,[1,2,5] Keyu Xia (夏可宇),[1,2§]
[1]*College of Engineering and Applied Sciences, National Laboratory of Solid State Microstructures, and Collaborative Innovation Center of Advanced Microstructures, Nanjing University, Nanjing 210023, China*
[2]*School of Physics, Nanjing University, Nanjing 210023, China*
[3]*School of Physics and Information Technology, Shaanxi Normal University, Xi'an 710062, China*
[4]*School of Science, Nanjing University of Science and Technology, Nanjing 210094, China*
[5]*Department of Physics, University of Arkansas, Fayetteville, Arkansas 72701, USA*

This supplementary material mainly provides details for the derivation of the effective photon-photon interaction strength η, the equal-time second-order autocorrelation function $g_s^{(2)}(0)$ and the yield and purity of heralded single-photon sources (HSPSs) for the case without considering the nonlinearity induced by photon blockade. We also discuss the influence of non-pair photon states, the cavity decay and π-pulse excitation. Finally, we use the quantum trajectory approach to study the statistical properties of the output photons from a single-mode cavity, a dual-mode cavity, our system shown in the main text.

I. THE EFFECTIVE PHOTON-PHOTON INTERACTION STRENGTH

In this section, we derive the effective photon-photon interaction (PPI) and the self-Kerr nonlinearity in two different kinds of N-type configurations using rubidium (Rb) atoms.

A. Type-I N-configuration of ^{87}Rb atoms

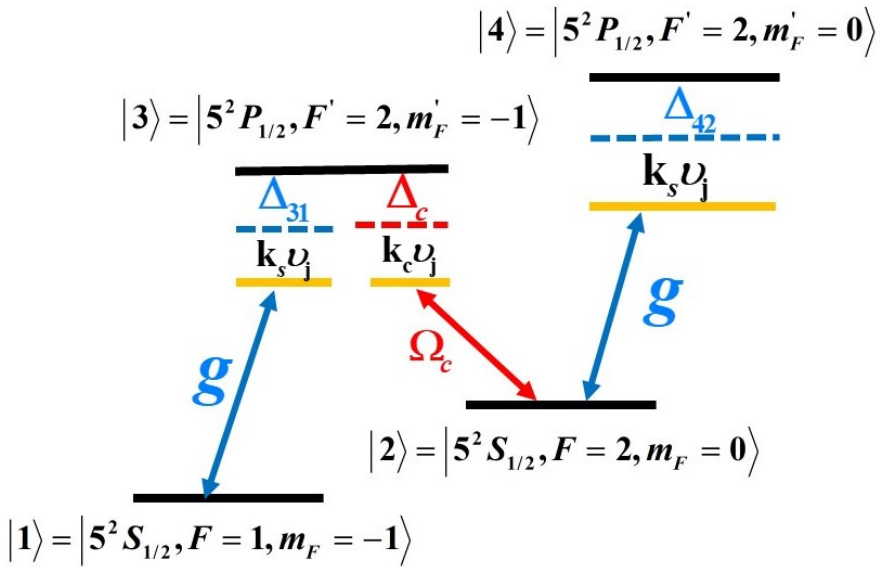

FIG. S1. Type-I N-configuration diagram of the ^{87}Rb atom. The cavity and atoms are coupled with a strength g. Without taking into account the microscopic Doppler effect, the cavity field drives the transitions $1 \leftrightarrow 3$ and $2 \leftrightarrow 4$ with detunings Δ_{31} and Δ_{42}, respectively. The control field drives the transition $2 \leftrightarrow 3$ with the detuning Δ_c and the Rabi frequency Ω_c.

The energy levels of N-type atom are denoted as $|l\rangle$ with eigenfrequency ω_l ($l = 1, 2, 3, 4$), as shown Fig. S1. In the this type-I configuration, we consider the cavity field couples with $1 \leftrightarrow 3$ and $2 \leftrightarrow 4$ transitions simultaneously.

The Hamiltonian of the system takes the form ($\hbar = 1$)

$$\begin{aligned} H_{tpye-I} =& \sum_{j=1}^{N}\sum_{l=1}^{4}\omega_l\sigma_{ll}^j + \omega_i a_i^\dagger a_i + \omega_s a_s^\dagger a_s \\ &+ \sum_{j=1}^{N}\left[g(a_s^\dagger\sigma_{13}^j + a_s^\dagger\sigma_{24}^j) + \Omega_c e^{i\omega_c t}\sigma_{23}^j + h.c.\right], \end{aligned} \tag{S1}$$

where a_i and a_s ($a_i^\dagger$ and $a_s^\dagger$) are the annihilation operators (creation operators) of idler photons and signal photons, respectively. $\sigma_{mn}^j = |m\rangle\langle n|$ ($m, n = 1, 2, 3, 4$) denotes the transition operator for the jth atom. The first line in Eq. (S1) is the free Hamiltonian of the system. The second line describes the atoms interact with the cavity and control fields, respectively. The last line represents the pump applied to the nonlinear crystal [1]. Note that the signal mode resonates with the cavity, while the idler mode decouples from atoms.

In the rotating frame, defined by an unitary transformation $U_1 = \exp\{i\sum_{j=1}^{N}[\omega_1\sigma_{11}^j + (\omega_s+\omega_1-\omega_c)\sigma_{22}^j + (\omega_s+\omega_1)\sigma_{33}^j + (2\omega_s+\omega_1-\omega_c)\sigma_{44}^j]t + i(\omega_i a_i^\dagger a_i + \omega_s a_s^\dagger a_s)t\}$, the Hamiltonian can be written as

$$\begin{aligned} H'_{type-I} =& \sum_{j=1}^{N}\Big[(-\Delta_{31}+\Delta_c)\sigma_{22}^j - \Delta_{31}\sigma_{33}^j + (-\Delta_{42}-\Delta_{31}+\Delta_c)\sigma_{44}^j)\Big] \\ &+ \sum_{j=1}^{N}\Big[g(a_s^\dagger\sigma_{13}^j + a_s^\dagger\sigma_{24}^j) + \Omega_c\sigma_{23}^j + h.c.\Big], \end{aligned} \tag{S2}$$

where $\sigma_{mn}^j = |m\rangle\langle n|$ and the superscript j represents the jth atom. $\Delta_{31} = \omega_s - \omega_{31}$ ($\Delta_{42} = \omega_s - \omega_{42}$) is the detuning between cavity and the transition of $|3\rangle \leftrightarrow |1\rangle$ ($|4\rangle \leftrightarrow |2\rangle$), and $\Delta_c = \omega_c - \omega_{32}$ is the detuning between the control field and the $|3\rangle \leftrightarrow |2\rangle$ transition in the absence of thermal motion ($\omega_{mn} = \omega_m - \omega_n$). The excited states $|m\rangle$ $(m = 3, 4)$ decay to the ground states $|n\rangle$ $(n = 1, 3)$ at a rate $\gamma_{m,n}$. The dephasing between the excited states $(m = 3, 4)$ and the ground states $(n = 1, 2)$ are represented by γ_{21} and γ_{43}, repectively. The decay and dephasing of the system can be described by the Lindblad operator:

$$\begin{aligned} \mathscr{L}O =& \frac{\gamma_{21}}{2}(2\sigma_{21}^j O\sigma_{12}^j - \sigma_{22}^j O - O\sigma_{22}^j) \\ &+ \frac{\gamma_{31}}{2}(2\sigma_{31}^j O\sigma_{13}^j - \sigma_{33}^j O - O\sigma_{33}^j) + \frac{\gamma_{32}}{2}(2\sigma_{32}^j O\sigma_{23}^j - \sigma_{33}^j O - O\sigma_{33}^j) \\ &+ \frac{\gamma_{41}}{2}(2\sigma_{41}^j O\sigma_{14}^j - \sigma_{44}^j O - O\sigma_{44}^j) + \frac{\gamma_{42}}{2}(2\sigma_{42}^j O\sigma_{24}^j - \sigma_{44}^j O - O\sigma_{44}^j) + \frac{\gamma_{43}}{2}(2\sigma_{43}^j O\sigma_{34}^j - \sigma_{44}^j O - O\sigma_{44}^j). \end{aligned} \tag{S3}$$

Then, the Heisenberg's equations for the system take the form

$$\dot{\sigma}_{11}^j = ig\sigma_{31}^j a_s - ig\sigma_{13}^j a_s^\dagger + \gamma_{41}\sigma_{44}^j + \gamma_{31}\sigma_{33}^j + \gamma_{21}\sigma_{22}^j\ , \tag{S4a}$$

$$\dot{\sigma}_{22}^j = -i(\Omega_c\sigma_{23}^j - \Omega_c^*\sigma_{32}^j) + ig(\sigma_{42}^j a_s - a_s^\dagger\sigma_{24}^j) + \gamma_{42}\sigma_{44}^j + \gamma_{32}\sigma_{33}^j - \gamma_{21}\sigma_{22}^j\ , \tag{S4b}$$

$$\dot{\sigma}_{33}^j = i(\Omega_c\sigma_{23}^j - \Omega_c^*\sigma_{32}^j) + ig(a_s^\dagger\sigma_{13}^j - \sigma_{31}^j a_s) + \gamma_{43}\sigma_{44}^j - \gamma_{31}\sigma_{33}^j - \gamma_{32}\sigma_{33}^j\ , \tag{S4c}$$

$$\dot{\sigma}_{44}^j = ig(a_s^\dagger\sigma_{24}^j - \sigma_{42}^j a_s) - (\gamma_{41}+\gamma_{42}+\gamma_{43})\sigma_{44}^j\ , \tag{S4d}$$

$$\dot{\sigma}_{31}^j = -i\Delta_{31}\sigma_{31}^j + iga_s^\dagger(\sigma_{11}^j - \sigma_{33}^j) + i\Omega_c\sigma_{21}^j - \frac{\gamma_{31}+\gamma_{32}}{2}\sigma_{31}^j\ , \tag{S4e}$$

$$\dot{\sigma}_{32}^j = -i\Delta_c\sigma_{32}^j + iga_s^\dagger(\sigma_{12}^j - \sigma_{34}^j) + i\Omega_c(\sigma_{22}^j - \sigma_{33}^j) - \frac{\gamma_{21}+\gamma_{31}+\gamma_{32}}{2}\sigma_{32}^j\ , \tag{S4f}$$

$$\dot{\sigma}_{21}^j = i(\Delta_c - \Delta_{31})\sigma_{21}^j + i\Omega_c^*\sigma_{31}^j + ig\sigma_{41}^j a_s - iga_s^\dagger\sigma_{23}^j - \frac{\gamma_{21}}{2}\sigma_{21}^j\ , \tag{S4g}$$

$$\dot{\sigma}_{41}^j = i(\Delta_c - \Delta_{31} - \Delta_{42})\sigma_{41}^j + iga_s^\dagger\sigma_{21}^j - iga_s^\dagger\sigma_{43}^j - \frac{\gamma_{41}+\gamma_{42}+\gamma_{43}}{2}\sigma_{41}^j\ , \tag{S4h}$$

$$\dot{\sigma}_{42}^j = -i\Delta_{42}\sigma_{42}^j + iga_s^\dagger(\sigma_{22}^j - \sigma_{44}^j) - i\Omega_c\sigma_{43}^j - \frac{\gamma_{21}+\gamma_{41}+\gamma_{42}+\gamma_{43}}{2}\sigma_{42}^j\ , \tag{S4i}$$

$$\dot{\sigma}_{43}^j = i(\Delta_c - \Delta_{42})\sigma_{43}^j + iga_s^\dagger\sigma_{23}^j - ig\sigma_{41}^j a_s - i\Omega_c^*\sigma_{42}^j - \frac{\gamma_{31}+\gamma_{32}+\gamma_{41}+\gamma_{42}+\gamma_{43}}{2}\sigma_{43}^j\ . \tag{S4j}$$

We can derive the self-Kerr nonlinearity from Eqs. (S4) by using the perturbation approach [2–4]. The transition operators can be expanded as $\sigma_{mn}^j = \sigma_{mn}^{j(0)} + \sigma_{mn}^{j(1)} + \sigma_{mn}^{j(2)} + \sigma_{mn}^{j(3)} + \cdots$. In our configuration, we have $g \ll \Omega_c$, to a good approximation, all the populations can be assumed in the ground state $|1\rangle$ to zeroth order, that is, $\sigma_{11}^{j(0)} = 1$, $\sigma_{22}^{j(0)} = \sigma_{33}^{j(0)} = \sigma_{44}^{j(0)} = 0$. Therefore, we also have $\sigma_{mn}^{j(0)} = 0$ $(m \neq n)$. The terms with $\sigma_{mn}^j g$ $(m \neq n)$ can be neglected when solving σ_{mn}^j. Solving Eqs. (S4), we obtain the first order solutions for the transition operators

$$\sigma_{21}^{j(1)} = -\frac{g\Omega_c^* a_s^\dagger}{F\tilde{\gamma}_{21}}\ , \tag{S5a}$$

$$\sigma_{31}^{j(1)} = -\frac{iga_s^\dagger}{F}\ , \tag{S5b}$$

with

$$F = \tilde{\gamma}_{31} + \frac{|\Omega_c|^2}{\tilde{\gamma}_{21}}. \tag{S6}$$

Where we define $\tilde{\gamma}_{21} = -i(\Delta_{31} - \Delta_c) - \gamma_{21}/2$, $\tilde{\gamma}_{31} = -i\Delta_{31} - (\gamma_{31} + \gamma_{32})/2$, $\tilde{\gamma}_{42} = -i\Delta_{42} - (\gamma_{21} + \gamma_{41} + \gamma_{42} + \gamma_{43})/2$, and $\tilde{\gamma}_{43} = -i(\Delta_{42} - \Delta_c) - (\gamma_{31} + \gamma_{32} + \gamma_{41} + \gamma_{42} + \gamma_{43})/2$ for simplicity. As for a closed system, the total population is conserved, i.e., $\sigma_{11}^j + \sigma_{22}^j + \sigma_{33}^j + \sigma_{44}^j = 1$. The second-order population operators satisfy the relationship

$$\sigma_{11}^{j(2)} + \sigma_{22}^{j(2)} + \sigma_{33}^{j(2)} + \sigma_{44}^{j(2)} = 0\,. \tag{S7}$$

Substituting Eqs. (S5) and Eq. (S7) to Eqs. (S4a-d), we obtain the second-order population operators

$$\sigma_{11}^{j(2)} = \frac{g^2 a_s^\dagger a_s(\gamma_{32} + \gamma_{21})}{\gamma_{21}(\gamma_{31} + \gamma_{32})}(\frac{1}{F} + \frac{1}{F^*})\,, \tag{S8a}$$

$$\sigma_{22}^{j(2)} = -\frac{g^2 a_s^\dagger a_s \gamma_{32}}{\gamma_{21}(\gamma_{31} + \gamma_{32})}(\frac{1}{F} + \frac{1}{F^*})\,, \tag{S8b}$$

$$\sigma_{33}^{j(2)} = -\frac{g^2 a_s^\dagger a_s}{\gamma_{31} + \gamma_{32}}(\frac{1}{F} + \frac{1}{F^*})\,. \tag{S8c}$$

Similarly, substituting Eqs. (S8) into Eqs. (S4e-j) and solving it, we obtain the third-order atomic polarizations

$$\sigma_{31}^{j(3)} = -\frac{ig^3 a_s^\dagger a_s^\dagger a_s(2\gamma_{21} + \gamma_{32})}{F\gamma_{21}(\gamma_{31} + \gamma_{32})}(\frac{1}{F} + \frac{1}{F^*})\,, \tag{S9a}$$

$$\sigma_{42}^{j(3)} = \frac{ig^3 a_s^\dagger a_s^\dagger a_s \gamma_{32}}{F_1\gamma_{21}(\gamma_{31} + \gamma_{32})}(\frac{1}{F} + \frac{1}{F^*})\,, \tag{S9b}$$

where

$$F_1 = \tilde{\gamma}_{42} + \frac{|\Omega_c|^2}{\tilde{\gamma}_{43}}. \tag{S10}$$

The first and third order approximations of σ_{32}^j are zero, i.e., $\sigma_{32}^{j(1)}$=$\sigma_{32}^{j(3)} = 0$. Because $\sigma_{22}^{j(0)} = \sigma_{22}^{j(1)} = \sigma_{22}^{j(3)} = 0$, $\sigma_{33}^{j(0)} = \sigma_{33}^{j(1)} = \sigma_{33}^{j(3)} = 0$, $\sigma_{44}^{j(0)} = \sigma_{44}^{j(1)} = \sigma_{44}^{j(2)} = \sigma_{44}^{j(3)} = 0$, $\sigma_{31}^{j(0)} = \sigma_{31}^{j(2)} = 0$, and $\sigma_{42}^{j(0)} = \sigma_{42}^{j(1)} = \sigma_{42}^{j(2)} = 0$, we have $\sigma_{22}^j \approx \sigma_{22}^{j(2)}$, $\sigma_{33}^j \approx \sigma_{33}^{j(2)}$, $\sigma_{44}^j \approx 0$, $\sigma_{31}^j \approx \sigma_{31}^{j(1)} + \sigma_{31}^{j(3)}$, and $\sigma_{42}^j \approx \sigma_{42}^{j(3)}$. Substituting these formulas for σ_{22}^j, σ_{33}^j, σ_{44}^j, σ_{31}^j and σ_{42}^j into the Hamiltonian Eq. S2, we obtain the effective Hamiltonian

$$H'_{\text{type-I,eff}} = \tilde{\Delta} a_s^\dagger a_s + \tilde{\eta} a_s^\dagger a_s^\dagger a_s a_s, \tag{S11}$$

with the nonlinear PPI strength,

$$\tilde{\eta} = \sum_{j=1}^{N}\left[\frac{ig^4(2\gamma_{21} + \gamma_{32})}{\gamma_{21}(\gamma_{31} + \gamma_{32})}(\frac{1}{F} + \frac{1}{F^*})(\frac{1}{F^*} - \frac{1}{F}) + \frac{ig^4\gamma_{32}}{\gamma_{21}(\gamma_{31} + \gamma_{32})}(\frac{1}{F} + \frac{1}{F^*})(\frac{1}{F_1} - \frac{1}{F_1^*})\right]\,, \tag{S12}$$

and a linear shift,

$$\tilde{\Delta} = \sum_{j=1}^{N}\left[\frac{g^2\gamma_{32}}{\gamma_{21}(\gamma_{31} + \gamma_{32})}(\frac{1}{F} + \frac{1}{F^*})(\Delta_{31} - \Delta_c) + \frac{g^2\Delta_{31}}{\gamma_{31} + \gamma_{32}}(\frac{1}{F} + \frac{1}{F^*}) + ig^2(\frac{1}{F^*} - \frac{1}{F})\right]\,. \tag{S13}$$

In our proposed scheme, the performance of single-photon source strongly depends on the photon blockade strength, i.e. the magnitude of the PPI strength η.

Next, we first consider N identical atoms and exclude the microscopic doppler effect. In the case of $\Omega_c \gg \gamma_0, g, \Delta_{31}$, Δ_c and Δ_{42}, the approximate analytical formula for the PPI strength η_0 can be derived from the Eq. (S12) as

$$\eta_{0,type-I} \approx \frac{2N_a g^4 \gamma_{32}}{|\Omega_c|^4(\gamma_{31} + \gamma_{32})}\left[\frac{2\gamma_{21} + \gamma_{32}}{\gamma_{32}}(\Delta_{31} - \Delta_c) - (\Delta_{42} - \Delta_c)\right]\,, \tag{S14}$$

where N_a is the total atom number. From this expression, we can see that when $\Omega_c \gg \Delta_{31}, \Delta_c$, the value of η_0 is proportional to $g/|\Omega_c|$. A large PPI can be achieved by adjusting the values of $g/|\Omega_c|$ and $|\Delta_{31} - \Delta_c|$. Here we take $\Delta_c = 0$ in the following calculation. The PPI strength can also be effectively adjusted by controlling the number of Rb atoms because $\eta_{0,type-I}$ is proportional to N_a.

Now we consider the Doppler effect of warm atoms. To do so, we replace Δ_{31}, Δ_c and Δ_{42} by $\Delta_{31} + k_s v$, $\Delta_c + k_c v$, and $\Delta_{42} + k_s v$, and $\sum_j \to \int dv$. Then the PPI strength and linear shift are given by

$$\begin{aligned}\eta = \int N(v)[&\frac{ig^4(2\gamma_{21}+\gamma_{32})}{\gamma_{21}(\gamma_{31}+\gamma_{32})}(\frac{1}{F(v)}+\frac{1}{F^*(v)})(\frac{1}{F^*(v)}-\frac{1}{F(v)}) \\ &+\frac{ig^4\gamma_{32}}{\gamma_{21}(\gamma_{31}+\gamma_{32})}(\frac{1}{F(v)}+\frac{1}{F^*(v)})(\frac{1}{F_1(v)}-\frac{1}{F_1^*(v)})]dv,\end{aligned} \tag{S15}$$

$$\begin{aligned}\Delta = \int N(v)[&\frac{g^2\gamma_{32}}{\gamma_{21}(\gamma_{31}+\gamma_{32})}(\frac{1}{F(v)}+\frac{1}{F^*(v)})(\Delta_{31}-\Delta_c+k_s v-k_c v) \\ &+\frac{g^2(\Delta_{31}+k_s v)}{\gamma_{31}+\gamma_{32}}(\frac{1}{F(v)}+\frac{1}{F^*(v)})+ig^2(\frac{1}{F^*(v)}-\frac{1}{F(v)})]dv,\end{aligned} \tag{S16}$$

where we have assumed that the atomic velocity obeys a Maxwell-Boltzmann distribution, i.e., $N(v) = N_a e^{-v^2/u^2}/u\sqrt{\pi}$.

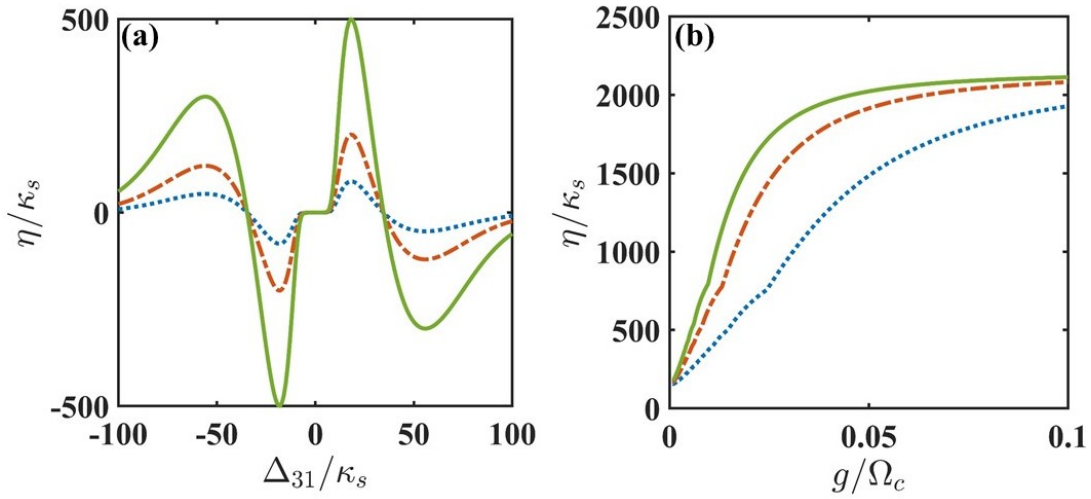

FIG. S2. (a) The effective PPI strength η as a function of the detuning Δ_{31} in type-I N-configuration. The parameters are $\gamma_{31} = \gamma_{32} = \gamma_{42} = \gamma_0 = 0.5\kappa_s$, $\gamma_{21} = 0.01\kappa_s$, $\Omega_c = 30\gamma_0$, $\Delta_{42} = 8.5\Delta_{31}$, $\Delta_c = 0$ and $N_a\,(g/\kappa_s)^4 = 0.92 \times 10^3$ [$N_a\,(g/\kappa_s)^4 = 2.3 \times 10^3$,$N_a\,(g/\kappa_s)^4 = 5.7 \times 10^3$] for the dotted blue curve (the dashed red curve, the solid green curve). (b) The PPI strength η versus g/Ω_c. We take the "optimal point" for η when scanning Δ_{31} for every g/Ω_c. The dotted blue (the dashed red, the solid blue) curve is calculated with $\Delta_c/\Delta_{31} = 0$ $(-2, -4)$ and $N\,(g/\kappa_s)^4 = 2.3 \times 10^3$ for both three curves. Other parameters are the same as (a).

Then, we estimate the available PPI strength in an ensemble of warm Rb atoms with the Doppler effect. The effective PPI strength is shown in Fig. S2. The PPI strength η has a "dispersive" profile and is zero in the vicinity of $\Delta_{31} = 0$. When the detuning Δ_{31} changes, there are always two maximum for the absolute value of the nonlinearity at $\Delta_{31}/\kappa_s = \pm 18$. For example, the absolute value of PPI strength can reach $|\eta|/\kappa_s = 80$ ($|\eta|/\kappa_s = 200$, $|\eta|/\kappa_s = 500$) when $N_a\,(g/\kappa_s)^4 = 0.92 \times 10^3$ ($N_a\,(g/\kappa_s)^4 = 2.3 \times 10^3$, $N_a\,(g/\kappa_s)^4 = 5.7 \times 10^3$). We call these points "optimal points". In Fig. S2(b), the available strongest nonlinearity increases as g/Ω_c, which is well understand and in consistent with the approximate formulas in Eq. (S14). However, when the increase of g/Ω_c is higher than about 0.05, the changes of the PPI strength η tend to be flat. This is because the conditions of $\Omega_c \gg \gamma_0, g, \Delta_{31}(\Delta_c)$ used in the approximation analysis gradually become invalid as Ω_c gets smaller. The terms we previously neglected have the opposite effect on the values of η, which gradually become non-negligible. In addition, we should also note that the premise of the perturbation method used in the model, i.e., $|g| \ll |\Omega_c|$, which is exactly contradictory to the increase of g/Ω_c. So the value of g/Ω_c cannot be increased indefinitely. There is a competitive relationship between making the perturbation approach effective and getting a large nonlinearity [5]. Moreover, increasing $|\Delta_c/\Delta_{31}|$ can also increase the value of

the PPI strength (see Fig. S2(b)). This large PPI allows us to achieve strong photon blockade for signal photons.

B. Type-II N-configuration of ^{87}Rb atoms

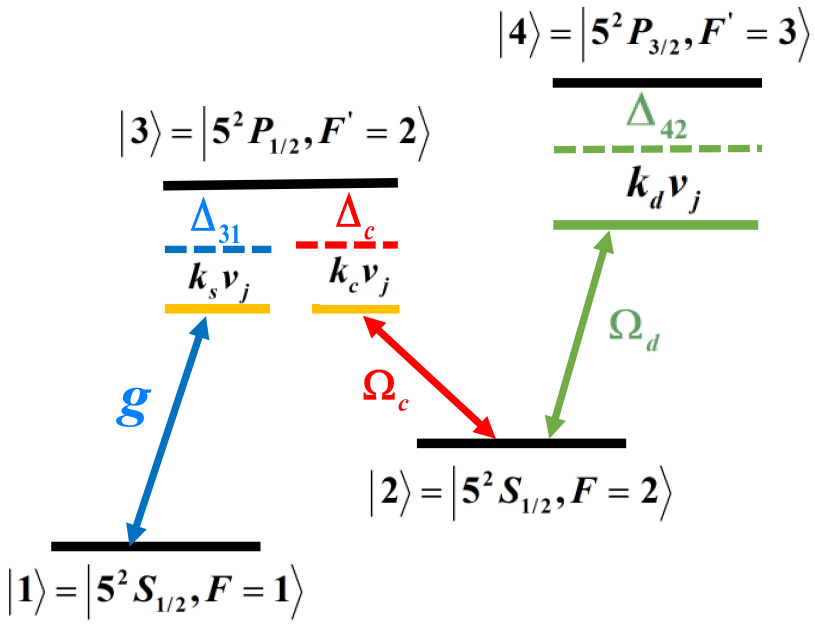

FIG. S3. Type-II N-configuration diagram of the ^{87}Rb atom. The signal photon (g), coupling field (Ω_c), and switching field (Ω_d) drive the transitions $1 \leftrightarrow 3$, $2 \leftrightarrow 3$ and $2 \leftrightarrow 4$, with detunings Δ_{31}, Δ_c and Δ_{42}, respectively.

The strong PPI can also be realized by using the N-type configuration of ^{87}Rb atom reported in [4], see Fig. S3 for level diagram. It has been experimentally demonstrated that strong adjustable self-Kerr nonlinearity can be achieved in this type-II N-configuration. The results given by the perturbation theory are in good agreement with experiments.

The Hamiltonian describing this N-configuration is

$$\begin{aligned} H_{type-II} = &\sum_{j=1}^{N}\left[(-\Delta_{31}+\Delta_c)\sigma_{22}^j - \Delta_{31}\sigma_{33}^j + (-\Delta_{42}-\Delta_{31}+\Delta_c)\sigma_{44}^j)\right] \\ &+ \sum_{j=1}^{N}\left[g(a_s^\dagger\sigma_{13}^j) + \Omega_d\sigma_{24}^j + \Omega_c\sigma_{23}^j + h.c.\right], \end{aligned} \tag{S17}$$

where $\Delta_{31} = \omega_s - \omega_{31}$, $\Delta_c = \omega_c - \omega_{32}$ and $\Delta_{42} = \omega_d - \omega_{42}$. ω_s, ω_c and ω_d represent the frequencies of signal, coupling and switching fields, respectively. The Lindblad equation of the system is the same as Eq. (S3) and the Heisenberg's

equations is

$$\dot{\sigma}_{11}^{j} = ig\sigma_{31}^{j}a_s - ig\sigma_{13}^{j}a_s^{\dagger} + \gamma_{41}\sigma_{44}^{j} + \gamma_{31}\sigma_{33}^{j} + \gamma_{21}\sigma_{22}^{j} \,, \tag{S18a}$$

$$\dot{\sigma}_{22}^{j} = -i(\Omega_c\sigma_{23}^{j} - \Omega_c^{*}\sigma_{32}^{j}) - i(\Omega_d\sigma_{42}^{j} - \Omega_d^{*}\sigma_{24}^{j}) + \gamma_{42}\sigma_{44}^{j} + \gamma_{32}\sigma_{33}^{j} - \gamma_{21}\sigma_{22}^{j} \,, \tag{S18b}$$

$$\dot{\sigma}_{33}^{j} = i(\Omega_c\sigma_{23}^{j} - \Omega_c^{*}\sigma_{32}^{j}) + ig(a_s^{\dagger}\sigma_{13}^{j} - \sigma_{31}^{j}a_s) + \gamma_{43}\sigma_{44}^{j} - \gamma_{31}\sigma_{33}^{j} - \gamma_{32}\sigma_{33}^{j} \,, \tag{S18c}$$

$$\dot{\sigma}_{44}^{j} = i(\Omega_d\sigma_{24}^{j} - \Omega_d^{*}\sigma_{42}^{j}) - (\gamma_{41} + \gamma_{42} + \gamma_{43})\sigma_{44}^{j} \,, \tag{S18d}$$

$$\dot{\sigma}_{31}^{j} = -i\Delta_{31}\sigma_{31}^{j} + iga_s^{\dagger}(\sigma_{11}^{j} - \sigma_{33}^{j}) + i\Omega_c\sigma_{21}^{j} - \frac{\gamma_{31} + \gamma_{32}}{2}\sigma_{31}^{j} \,, \tag{S18e}$$

$$\dot{\sigma}_{32}^{j} = -i\Delta_c\sigma_{32}^{j} + iga_s^{\dagger}\sigma_{12}^{j} - i\Omega_d\sigma_{34}^{j} + i\Omega_c(\sigma_{22}^{j} - \sigma_{33}^{j}) - \frac{\gamma_{21} + \gamma_{31} + \gamma_{32}}{2}\sigma_{32}^{j} \,, \tag{S18f}$$

$$\dot{\sigma}_{21}^{j} = i(\Delta_c - \Delta_{31})\sigma_{21}^{j} + i\Omega_c^{*}\sigma_{31}^{j} + i\Omega_d^{*}\sigma_{41}^{j} - iga_s^{\dagger}\sigma_{23}^{j} - \frac{\gamma_{21}}{2}\sigma_{21}^{j} \,, \tag{S18g}$$

$$\dot{\sigma}_{41}^{j} = i(\Delta_c - \Delta_{31} - \Delta_{42})\sigma_{41}^{j} + i\Omega_d\sigma_{21}^{j} - iga_s^{\dagger}\sigma_{43}^{j} - \frac{\gamma_{41} + \gamma_{42} + \gamma_{43}}{2}\sigma_{41}^{j} \,, \tag{S18h}$$

$$\dot{\sigma}_{42}^{j} = -i\Delta_{42}\sigma_{42}^{j} + i\Omega_d(\sigma_{22}^{j} - \sigma_{44}^{j}) - i\Omega_c\sigma_{43}^{j} - \frac{\gamma_{21} + \gamma_{41} + \gamma_{42} + \gamma_{43}}{2}\sigma_{42}^{j} \,, \tag{S18i}$$

$$\dot{\sigma}_{43}^{j} = i(\Delta_c - \Delta_{42})\sigma_{43}^{j} + i\Omega_d\sigma_{23}^{j} - ig\sigma_{41}^{j}a_s - i\Omega_c^{*}\sigma_{42}^{j} - \frac{\gamma_{31} + \gamma_{32} + \gamma_{41} + \gamma_{42} + \gamma_{43}}{2}\sigma_{43}^{j} \,. \tag{S18j}$$

Solve the Eqs. (S18a) using the same approach above, we can obtain the first order solutions

$$\sigma_{21}^{j(1)} = -\frac{\Omega_c^{*}g\tilde{\gamma}_{41}}{\tilde{\gamma}_{21}\tilde{\gamma}_{41} + |\Omega_d|^2}a_s^{\dagger} \,, \tag{S19a}$$

$$\sigma_{31}^{j(1)} = -\frac{ig}{F_3}a_s^{\dagger} \,, \tag{S19b}$$

$$\sigma_{41}^{j(1)} = \frac{i\Omega_d\Omega_c^{*}g}{\tilde{\gamma}_{21}\tilde{\gamma}_{41} + |\Omega_d|^2}a_s^{\dagger} \,, \tag{S19c}$$

with

$$F_3 = \tilde{\gamma}_{31} + \frac{\tilde{\gamma}_{41}|\Omega_c|^2}{\tilde{\gamma}_{21}\tilde{\gamma}_{41} + |\Omega_d|^2}. \tag{S20}$$

Where $\tilde{\gamma}_{21} = -i(\Delta_{31} - \Delta_c) - \gamma_{21}/2$, $\tilde{\gamma}_{31} = -i\Delta_{31} - (\gamma_{31} + \gamma_{32})/2$, and $\tilde{\gamma}_{41} = i(\Delta_c - \Delta_{31} - \Delta_{42}) - (\gamma_{41} + \gamma_{42} + \gamma_{43})/2$. Using the closed system condition, $\sigma_{11}^{j(2)} + \sigma_{22}^{j(2)} + \sigma_{33}^{j(2)} + \sigma_{44}^{j(2)} = 0$, and substituting Eqs. (19) into Eqs. (18 a-d), we get the second-order population operators

$$\sigma_{11}^{j(2)} = \frac{g^2(\gamma_{32} + \gamma_{21})}{\gamma_{21}(\gamma_{31} + \gamma_{32})}(\frac{1}{F_3} + \frac{1}{F_3^{*}})a_s^{\dagger}a_s \,, \tag{S21a}$$

$$\sigma_{22}^{j(2)} = -\frac{g^2\gamma_{32}}{\gamma_{21}(\gamma_{31} + \gamma_{32})}(\frac{1}{F_3} + \frac{1}{F_3^{*}})a_s^{\dagger}a_s \,, \tag{S21b}$$

$$\sigma_{33}^{j(2)} = -\frac{g^2}{(\gamma_{31} + \gamma_{32})}(\frac{1}{F_3} + \frac{1}{F_3^{*}})a_s^{\dagger}a_s \,. \tag{S21c}$$

Similarly, substituting Eqs. (S21) into Eqs. (S18 e-j) and solving it, we obtain the third-order atomic polarizations

$$\sigma_{31}^{j(3)} = -\frac{ig^3(2\gamma_{21} + \gamma_{32})}{F_3\gamma_{21}(\gamma_{31} + \gamma_{32})}(\frac{1}{F_3} + \frac{1}{F_3^{*}})a_s^{\dagger}a_s^{\dagger}a_s. \tag{S22}$$

The first and third order approximations of σ_{32}^{j} are zero, i.e., $\sigma_{32}^{j(1)}$=$\sigma_{32}^{j(3)} = 0$. Because $\sigma_{22}^{j(0)} = \sigma_{22}^{j(1)} = \sigma_{22}^{j(3)} = 0$, $\sigma_{33}^{j(0)} = \sigma_{33}^{j(1)} = \sigma_{33}^{j(3)} = 0$, $\sigma_{44}^{j(0)} = \sigma_{44}^{j(1)} = \sigma_{44}^{j(2)} = \sigma_{44}^{j(3)} = 0$, $\sigma_{31}^{j(0)} = \sigma_{31}^{j(2)} = 0$, and $\sigma_{42}^{j(0)} = \sigma_{42}^{j(1)} = \sigma_{42}^{j(2)} = \sigma_{42}^{j(3)} = 0$, we have $\sigma_{22}^{j} \approx \sigma_{22}^{j(2)}$, $\sigma_{33}^{j} \approx \sigma_{33}^{j(2)}$, $\sigma_{44}^{j} \approx 0$, $\sigma_{42}^{j} \approx 0$, and $\sigma_{31}^{j} \approx \sigma_{31}^{j(1)} + \sigma_{31}^{j(3)}$. Substituting these formulas for σ_{22}^{j}, σ_{33}^{j}, σ_{44}^{j}, and σ_{31}^{j} into the Hamiltonian Eq. (S17), we can obtain the effective Hamiltonian

$$H_{\text{type-II,eff}} = \tilde{\Delta}a_s^{\dagger}a_s + \tilde{\eta}a_s^{\dagger}a_s^{\dagger}a_sa_s, \tag{S23}$$

with the nonlinear interaction strength,

$$\tilde{\eta} = iX_0 \sum_{j=1}^{N} (\frac{1}{F_3} + \frac{1}{F_3^*})(\frac{1}{F_3^*} - \frac{1}{F_3}), \tag{S24}$$

and a linear shift,

$$\tilde{\Delta} = \sum_{j=1}^{N} g^2 \left[\frac{\gamma_{32}}{\gamma_{21}(\gamma_{31}+\gamma_{32})} (\frac{1}{F_3} + \frac{1}{F_3^*})(\Delta_{31} - \Delta_c) + \frac{\Delta_{31}}{(\gamma_{31}+\gamma_{32})} (\frac{1}{F_3} + \frac{1}{F_3^*}) + i(\frac{1}{F_3^*} - \frac{1}{F_3}) \right], \tag{S25}$$

where $X_0 = g^4(2\gamma_{21} + \gamma_{32})/\left[\gamma_{21}(\gamma_{31}+\gamma_{32})\right]$. Again, we first consider N identical atoms and exclude the microscopic doppler effect. In the case of $\Omega_c \gg \gamma_0, g,$ and Ω_d, the approximate expressions of the PPI strength $\eta_{0,type-II}$ from the Eq. (S24) can be solved as

$$\eta_{0,type-II} \approx \frac{2N_a g^4(2\gamma_{21}+\gamma_{32})}{|\Omega_c|^4(\gamma_{31}+\gamma_{32})}(\Delta_{31} - \Delta_c). \tag{S26}$$

From the formula Eq. (S26), we can see that the PPI strength can also be effectively adjusted by controlling the number of Rb atoms N_a.

Then, we consider the atomic Doppler effect and have

$$\eta = iX_0 \int (\frac{1}{F_3(v)} + \frac{1}{F_3^*(v)})(\frac{1}{F_3^*(v)} - \frac{1}{F_3(v)}) N(v) dv, \tag{S27}$$

$$\begin{aligned} \Delta = \int N(v) g^2 [& \frac{\gamma_{32}}{\gamma_{21}(\gamma_{31}+\gamma_{32})} (\frac{1}{F_3(v)} + \frac{1}{F_3^*(v)})(\Delta_{31} - \Delta_c + k_s v - k_c v) \\ & + \frac{(\Delta_{31} + k_s v)}{\gamma_{31}+\gamma_{32}} (\frac{1}{F_3(v)} + \frac{1}{F_3^*(v)}) + i(\frac{1}{F_3^*(v)} - \frac{1}{F_3(v)})] dv. \end{aligned} \tag{S28}$$

$$\begin{aligned} F_3(v) = & \frac{[i(\Delta_c - \Delta_{31} - \Delta_{42} - kv) - (\gamma_{41}+\gamma_{42}+\gamma_{43})/2]\,|\Omega_c|^2}{\{[(i(\Delta_c - \Delta_{31}) - \gamma_{21}/2)(i(\Delta_c - \Delta_{31} - \Delta_{42} - kv)] - (\gamma_{41}+\gamma_{42}+\gamma_{43})/2)\} + |\Omega_d|^2} \\ & - [(\Delta_{31} + kv) + (\gamma_{31}+\gamma_{32})/2]\,. \end{aligned} \tag{S29}$$

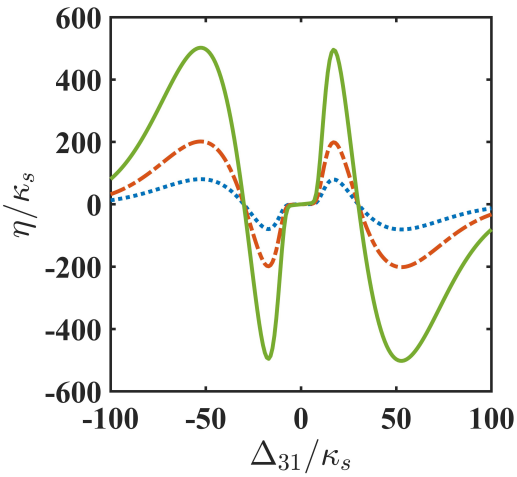

FIG. S4. The effective PPI strength η as a function of the detuning Δ_{31} in type-II N-configuration of ^{87}Rb atoms. The parameters are $\gamma_{31} = \gamma_{32} = \gamma_{42} = \gamma_0 = 0.5\kappa_s$, $\gamma_{21} = 0.01\kappa_s$, $\Omega_c = 30\gamma_0$, $\Omega_d = 3\gamma_0$, $\Delta_{42} = \Delta_c = 0$, and $N_a\,(g/\kappa_s)^4 = 1.3 \times 10^3$ [$N_a\,(g/\kappa_s)^4 = 3.25 \times 10^3$,$N_a\,(g/\kappa_s)^4 = 8.1 \times 10^3$] for the dotted blue curve (the dashed red curve, the solid green curve).

We set $\Delta_{42}=0$ and $\Delta_c=0$, which is the same as in [4] for the ^{87}Rb atomic N-configuration in Fig. S3. Figure. S4 shows the effective PPI strength as a function of the detuning Δ_{31}. When the detuning Δ_{31} changes, the PPI strength induced by the type-II N-configuration has two more "optimal points" to choose from than the type-I for a given number of atoms. For example, when $N_a(g/\kappa_s)^4=1.3\times10^3$ ($N_a(g/\kappa_s)^4=3.25\times10^3$, $N_a(g/\kappa_s)^4=8.1\times10^3$), the PPI strength η can reach $80\kappa_s$ ($200\kappa_s$, $500\kappa_s$) not only at $\Delta_{31}/\kappa_s=\pm18$, but also about at $\Delta_{31}/\kappa_s=\pm53$. At the same time, the two additional "optimal points" have a wider adjustable detuning range about $6\kappa_s$ in the vicinity of $\Delta_{31}/\kappa_s=\pm53$ than $2\kappa_s$ in the vicinity of $\Delta_{31}/\kappa_s=\pm18$ for $\eta/\kappa_s=80$ when $N_a(g/\kappa_s)^4=1.3\times10^3$. However, the type-II N-configuration requires a larger atomic density than the type-I to achieve the same nonlinear strength.

C. Hamiltonian of the full system

The Hamiltonian of the system including the SPDC process can be generally written as

$$H_{\text{full}}=\Delta a_s^\dagger a_s+\eta a_s^\dagger a_s^\dagger a_s a_s+\xi\sqrt{P}[e^{-i(\omega_p-\omega_i-\omega_s)t}a_i^\dagger a_s^\dagger+e^{i(\omega_p-\omega_i-\omega_s)t}a_i a_s].$$

Similarly, applying an unitary transformation of $U_2=exp\{-i(\omega_p-\omega_i-\omega_s)a_s^\dagger a_s t\}$ to the system, we can get the effective Hamiltonian

$$H_{\text{eff}}=(\Delta-\eta-\Delta_p)a_s^\dagger a_s+\eta(a_s^\dagger a_s)^2+\xi\sqrt{P}(a_i^\dagger a_s^\dagger+a_i a_s).$$

It is Eq. (2) in the main text.

II. THE EQUAL-TIME SECOND-ORDER AUTOCORRELATION FUNCTION

In this section, we derive the equal time second-order autocorrelation function conditional on the detection of the idler photons. The single-photon statistics from a HSPS by heralding detection of idler photons have been reported in [6] for the first time. For a heralding single-photon detection system, the state of the system can be described by density matrix. Once idler photons are detected, the system state degrades to ρ_s [7, 8]. In this case, the number states of the idler mode no longer have the contribution of the vacuum state, the probability of n_s photon becomes

$$\alpha_{n_s}=\langle n_s|\rho_s|n_s\rangle=\frac{\sum\limits_{n_i>0}P_{n_s,n_i}}{\sum\limits_{n_s',n_i'>0}P_{n_s',n_i'}}. \tag{S30}$$

When the idler photons are detected, the equal time second-order autocorrelation function of signal mode is given by

$$g_s^{(2)}(0)=\frac{\langle a_s^\dagger a_s^\dagger a_s a_s\rangle_i}{\langle a_s^\dagger a_s\rangle_i^2}, \tag{S31}$$

where $\langle\cdots\rangle_i$ is the average over the postmeasurement state when an idler photon is measured. And it can be calculated as

$$\begin{aligned}
\left\langle a_s^\dagger a_s^\dagger a_s a_s\right\rangle_i=\left\langle\psi_s\left|a_s^\dagger a_s^\dagger a_s a_s\right|\psi_s\right\rangle&=\sum_{n_s,n_s'}\langle\psi_s\mid n_s\rangle\left\langle n_s\left|a_s^\dagger a_s^\dagger a_s a_s\right|n_s'\right\rangle\langle n_s'\mid\psi_s\rangle\\
&=\sum_{n_s,n_s'}\langle n_s'\mid\psi_s\rangle\langle\psi_s\mid n_s\rangle\left\langle n_s\left|a_s^\dagger a_s^\dagger a_s a_s\right|n_s'\right\rangle\\
&=\sum_{n_s,n_s'}\langle n_s'\mid\psi_s\rangle\langle\psi_s\mid n_s\rangle n_s'\left(n_s'-1\right)\delta_{n_s,n_s'}\\
&=\sum_{n_s}\langle n_s\mid\psi_s\rangle\langle\psi_s\mid n_s\rangle n_s(n_s-1)\\
&=\sum_{n_s}\langle n_s\left|\rho_s\right|n_s\rangle n_s(n_s-1)\\
&=\sum_{n_s}n_s(n_s-1)\alpha_{n_s},
\end{aligned} \tag{S32}$$

$$\begin{aligned}\left\langle a_s^\dagger a_s\right\rangle_i = \left\langle \psi_s \left| a_s^\dagger a_s \right| \psi_s \right\rangle &= \sum_{n_s,n_s'} \langle\psi_s|n_s\rangle\langle n_s|a_s^\dagger a_s|n_s'\rangle\langle n_s'|\psi_s\rangle \\ &= \sum_{n_s,n_s'} \langle n_s'|\psi_s\rangle\langle\psi_s|n_s\rangle\langle n_s|a_s^\dagger a_s|n_s'\rangle \\ &= \sum_{n_s,n_s'} \langle n_s'|\psi_s\rangle\langle\psi_s|n_s\rangle n_s' \delta_{n_s,n_s'} \\ &= \sum_{n_s} \langle n_s|\psi_s\rangle \langle\psi_s|n_s\rangle n_s \\ &= \sum_{n_s} \langle n_s \left|\rho_s\right| n_s\rangle n_s \\ &= \sum_{n_s} n_s \alpha_{n_s}.\end{aligned} \tag{S33}$$

Substituting Eq. S32 and Eq. S33 into Eq. S31, we obtain

$$g_s^{(2)}(0) = \frac{\sum\limits_{n_s} n_s\left(n_s-1\right)\alpha_{n_s}}{\left(\sum\limits_{n_s} n_s\alpha_{n_s}\right)^2} = \frac{\left[\sum\limits_{n_s,n_i>0} n_s\left(n_s-1\right)P_{n_s,n_i}\right]\left(\sum\limits_{n_s,n_i>0} P_{n_s,n_i}\right)}{\left(\sum\limits_{n_s,n_i>0} n_s P_{n_s,n_i}\right)^2}. \tag{S34}$$

When the pump power and the PPI strength are very strong, the probability of multi-photon states can be neglected. In this case, $g_s^{(2)}(0) \approx 2\alpha_2/\alpha_1^2 \approx 2(P_{21}+P_{22})(P_{11}+P_{12}+P_{21}+P_{22})/(P_{11}+P_{12})^2$. Considering the main contribution of photon-pair states (nonphoton-pair states are discussed below), $g_s^{(2)}(0) \approx 2P_{22}/P_{11}$.

The purity, denoted as Π, of heralded single photons is usually defined as [9]

$$\Pi = \frac{\sum\limits_{n_i>0} P_{1,n_i}}{\sum\limits_{n_s'>0,n_i'>0} P_{n_s',n_i'}}. \tag{S35}$$

When the probability of single-photon pair is much greater than those of the multi-photon pairs, considering the main contribution of photon-pair states, we obtain

$$\Pi \approx P_{11}/(P_{11}+P_{22}) \approx 1 - P_{22}/P_{11}\ . \tag{S36}$$

In the case of $P_{11} \gg P_{22}$, we have

$$1 - g_s^{(2)}(0) = 1 - 2P_{22}/P_{11} \approx \Pi\ . \tag{S37}$$

Because $g_s^{(2)}(0)$ can be measured experimentally, $1-g_s^{(2)}(0)$ is usually used to characterize the heralded single-photon purity [10].

III. NON-BLOCKADE CASE

In this section, we discuss the non-blockade case, that is , without considering the PPI in our system. We derive the analytical expressions for the yield and purity of HSPS, and discuss the limitation on the yield and purity.

A. The Yield and Purity of HSPS

When PPI is not considered, the Hamiltonian of the system can be written as

$$H_0 = \xi\sqrt{P}(a_i^\dagger a_s^\dagger + a_i a_s). \tag{S38}$$

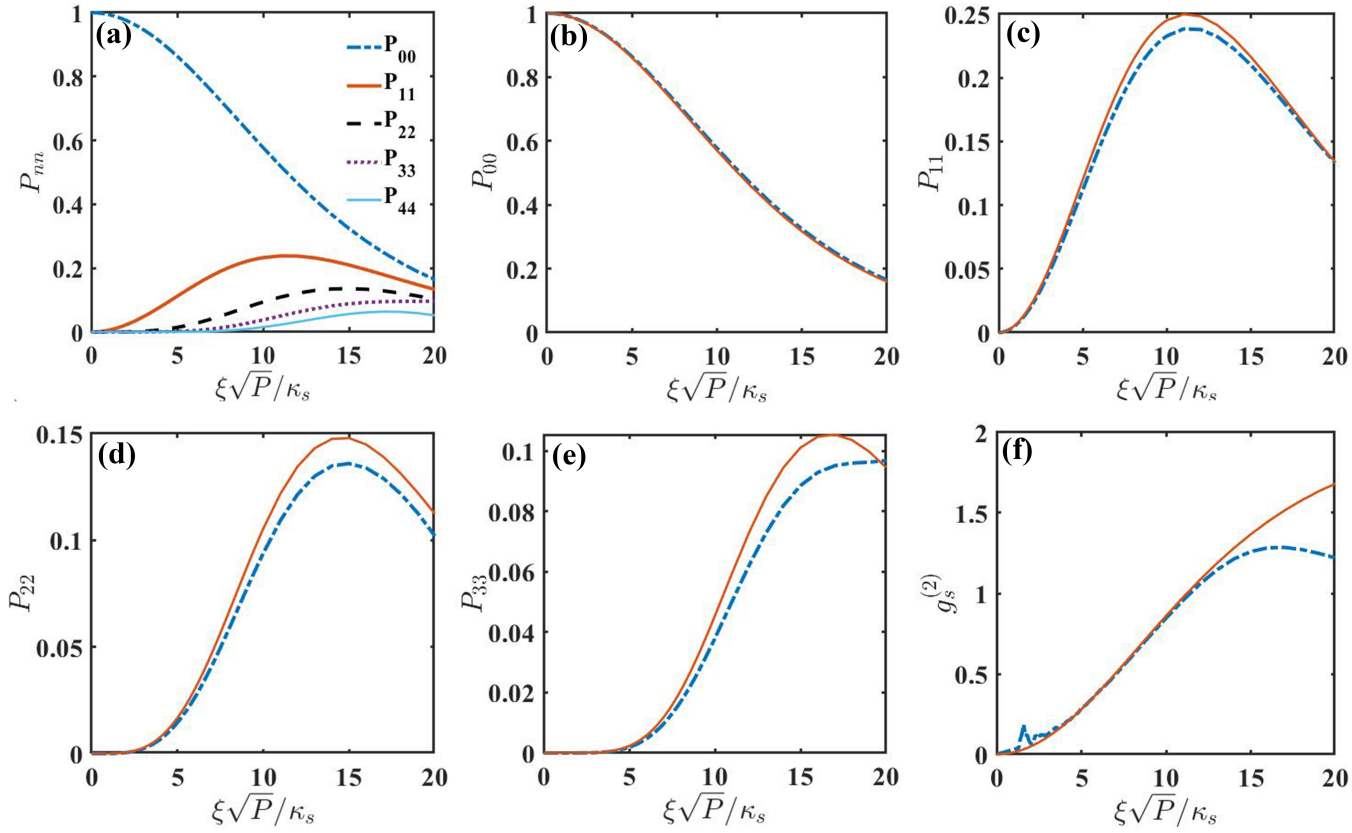

FIG. S5. (a) The numerical solutions of population of Fock states $|n_s, n_i\rangle$ as a function of the effective pump power $\xi\sqrt{P}$. (b-e) Comparison of numerical (dash-dotted curves) and analytical solutions (solid curves) of photon-pair population of P_{n_s,n_i} ($n_s = n_s = 0, 1, 2, 3$ for (b), (c), (d) and (e), respectively). (f) The equal time second-order autocorrelation $g_s^{(2)}$ versus the effective pump power $\xi\sqrt{P}$. Other parameters are $\kappa_s\tau_p = \pi/40$, $\kappa_s = \kappa_i = 1$.

One can show that, without considering the dissipation of photons, it creates the following two-mode entangled state [1]:

$$\begin{aligned} e^{-iH_0t}|0,0\rangle &= \frac{1}{\cosh(\xi\sqrt{P}t)} e^{-i\tanh(\xi\sqrt{P})a_i^\dagger a_s^\dagger}|0,0\rangle \\ &= \frac{1}{\cosh(\xi\sqrt{P}t)} \sum_{n=0}^{\infty} (-i)^n \tanh^n(\xi\sqrt{P}t)|n,n\rangle. \end{aligned} \tag{S39}$$

Here, to consistent with the main text, the Fock-state subscripts have been omitted. Then the probability of n-th pair is

$$P_{n,n} = \frac{\tanh^{2n}(\xi\sqrt{P}t)}{\cosh^2(\xi\sqrt{P}t)}. \tag{S40}$$

The yield of the heralded single-photon source (HSPS) can be measured by P_{11}, which means each pump laser pulse generating a single photon [11]. We use Y to represent the yield of the HSPS, then

$$Y = P_{11} = \frac{\tanh^2(\xi\sqrt{P}t)}{\cosh^2(\xi\sqrt{P}t)}. \tag{S41}$$

The heralded second-order autocorrelation function can be derived from Eq. (S34). Here, we only consider the

contribution of photon-pair states, i.e., $n_s = n_i$, we have

$$\alpha_{n_s} = \frac{\tanh^{2n_s}(\xi\sqrt{P}t)}{\left[\tanh^2(\xi\sqrt{P}t) + \tanh^4(\xi\sqrt{P}t) + \tanh^6(\xi\sqrt{P}t) + \cdots\right]}, \tag{S42}$$

and

$$g_s^{(2)}(0) = \frac{\sum\limits_{n_s} n_s(n_s-1)\alpha_{n_s}}{(\sum\limits_{n_s} n_s\alpha_{n_s})^2} = \frac{\left[\sum\limits_{n_s} n_s(n_s-1)\tanh^{2n_s}(\xi\sqrt{P}t)\right]\left[\sum\limits_{n_s>0}\tanh^{2n_s}(\xi\sqrt{P}t)\right]}{\left[\sum\limits_{n_s} n_s\tanh^{2n_s}(\xi\sqrt{P}t)\right]^2}, \tag{S43}$$

where:

$$\sum_{n_s>0}\tanh^{2n_s}(\xi\sqrt{P}t) = \frac{\tanh^2(\xi\sqrt{P}t)}{1-\tanh^2(\xi\sqrt{P}t)}, \tag{S44}$$

$$\begin{aligned}
\sum_{n_s} n_s\tanh^{2n_s}(\xi\sqrt{P}t) &= \frac{1}{2}\cosh^2(\xi\sqrt{P}t)\tanh(\xi\sqrt{P}t)\sum_{n_s}\frac{\partial}{\partial(\xi\sqrt{P}t)}\tanh^{2n_s}(\xi\sqrt{P}t) \\
&= \frac{1}{2}\cosh^2(\xi\sqrt{P}t)\tanh(\xi\sqrt{P}t)\frac{\partial}{\partial(\xi\sqrt{P}t)}\sum_{n_s}\tanh^{2n_s}(\xi\sqrt{P}t) \\
&= \frac{1}{2}\cosh^2(\xi\sqrt{P}t)\tanh(\xi\sqrt{P}t)\frac{\partial}{\partial(\xi\sqrt{P}t)}\left[\frac{1}{1-\tanh^2(\xi\sqrt{P}t)}\right] \\
&= \frac{\tanh^2(\xi\sqrt{P}t)}{\left[1-\tanh^2(\xi\sqrt{P}t)\right]^2}.
\end{aligned} \tag{S45}$$

Substituting Eq. (S44) and Eq. (S45) into Eq. (S43), we can obtain

$$g_s^{(2)}(0) = \frac{\left[\sum\limits_{n_s} n_s(n_s-1)\tanh^{2n_s}(\xi\sqrt{P}t)\right]\left[1-\tanh^2(\xi\sqrt{P}t)\right]^3}{\tanh^2(\xi\sqrt{P}t)}. \tag{S46}$$

When we consider the larger area of the pump pulse, i.e., $\xi\sqrt{P}t \gg 0$, we have

$$\begin{aligned}
(\frac{\partial}{\partial(\xi\sqrt{P}t)})^2\sum_{n_s}\tanh^{2n_s}(\xi\sqrt{P}t) &= \sum_{n_s}(\frac{\partial}{\partial(\xi\sqrt{P}t)})^2\tanh^{2n_s}(\xi\sqrt{P}t) \\
&= \sum_{n_s}(\frac{\partial}{\partial(\xi\sqrt{P}t)})\{2n_s\left[\tanh^{2n_s-2}(\xi\sqrt{P}t)\right]\cosh^{-2}(\xi\sqrt{P}t)\tanh(\xi\sqrt{P}t)\} \\
&= \sum_{n_s}\left[2\cosh^{-2}(\xi\sqrt{P}t)\tanh(\xi\sqrt{P}t)\right]\frac{\partial}{\partial(\xi\sqrt{P}t)}\left[n_s\tanh^{2n_s-2}(\xi\sqrt{P}t)\right] \\
&\quad + \sum_{n_s}\frac{\partial}{\partial(\xi\sqrt{P}t)}\left[\cosh^{-2}(\xi\sqrt{P}t)\tanh(\xi\sqrt{P}t)\right]\left[2n_s\tanh^{2n_s-2}(\xi\sqrt{P}t)\right].
\end{aligned} \tag{S47}$$

We can prove that the last row is approximately zero in the case of $\xi\sqrt{P}t \gg 0$, that is

$$\begin{aligned}\sum_{n_s}\frac{\partial}{\partial(\xi\sqrt{P}t)}&\left[\cosh^{-2}(\xi\sqrt{P}t)\tanh(\xi\sqrt{P}t)\right]\left[2n_s\tanh^{2n_s-2}(\xi\sqrt{P}t)\right]\\&=\sum_{n_s}\left[2\cosh^{-4}(\xi\sqrt{P}t)\sinh^2(\xi\sqrt{P}t)+\cosh^{-4}(\xi\sqrt{P}t)\right]\left[2n_s\tanh^{2n_s-2}(\xi\sqrt{P}t)\right]\\&\approx 0\quad(\xi\sqrt{P}t\gg 0),\end{aligned}\tag{S48}$$

so

$$\begin{aligned}(\frac{\partial}{\partial(\xi\sqrt{P}t)})^2\sum_{n_s}\tanh^{2n_s}(\xi\sqrt{P}t)&=\sum_{n_s}\left[2\cosh^{-2}(\xi\sqrt{P}t)\tanh(\xi\sqrt{P}t)\right]\frac{\partial}{\partial(\xi\sqrt{P}t)}\left[n_s\tanh^{2n_s-2}(\xi\sqrt{P}t)\right]\\&=\sum_{n_s}4n_s(n_s-1)\tanh^{2n_s}(\xi\sqrt{P}t)\cosh^{-4}(\xi\sqrt{P}t)\tanh^{-2}(\xi\sqrt{P}t),\end{aligned}\tag{S49}$$

and

$$\begin{aligned}\sum_{n_s}n_s(n_s-1)\tanh^{2n_s}(\xi\sqrt{P}t)&=\frac{1}{4}\cosh^4(\xi\sqrt{P}t)\tanh^2(\xi\sqrt{P}t)(\frac{\partial}{\partial(\xi\sqrt{P}t)})^2\sum_{n_s}\tanh^{2n_s}(\xi\sqrt{P}t)\\&=\frac{2\tanh^4(\xi\sqrt{P}t)}{\left[1-\tanh^2(\xi\sqrt{P}t)\right]^3}.\end{aligned}\tag{S50}$$

Substituting Eq. (S50) into Eq. (S46), we can easily obtain

$$g_s^{(2)}(0)\approx\frac{2\tanh^4(\xi\sqrt{P}t)}{\left[1-\tanh^2(\xi\sqrt{P}t)\right]^3}\cdot\frac{\left[1-\tanh^2(\xi\sqrt{P}t)\right]^3}{\tanh^2(\xi\sqrt{P}t)}=2\tanh^2(\xi\sqrt{P}t).\tag{S51}$$

The equal time second-order autocorrelation function can characterize the single-photon purity of a light field [11]. In our system based on idler-detection events, the purity of signal photons can be defined by [10]

$$\Pi=\begin{cases}1-g_s^{(2)}(0), & g_s^{(2)}(0)\le 1,\\ 0, & g_s^{(2)}(0)>1.\end{cases}\tag{S52}$$

In Fig. S5, we show the analytical and numerical solutions of the photon-pair population and the equal time second-order autocorrelation $g_s^{(2)}(0)$ as a function of the effective pump power $\xi\sqrt{P}$ without considering the photon blockade. The duration of pump laser is represented by τ_p and is fixed at $\kappa_s\tau_p=\pi/40$. Fig. S5(a) shows the numerical solutions of photon-pair populations P_{n_s,n_i} using the master equation. The analytical solutions in Fig. S5(b-e) use Eq. (S40), and the analytical solutions in Fig. S5(f) use Eq. (S51). We can find that in the low Fock states, the analytical and numerical solutions agree very well [see Fig. S5(b,c)]. The probability of single-photon pair has a maximum value of about 0.25 at $\xi\sqrt{P}/\kappa_s=11$. This spontaneous nature of the pair generation fundamentally limits the improvement of single-photon yield. When the Fock states are high, some deviations occur between the analytical and numerical solutions at high pump power [see Fig. S5(d,e)]. This is because the influence of the truncated space of photon number in our simulation calculation. When the pump power becomes larger, the excitation of multi-photon states increase gradually. Due to the limitation of truncated photon number space N_0, the effect of higher states is neglected, i.e., $O(N)(N>N_0)$. Therefore, the simulated value is slightly less than the theoretical value.

In our numerical simulation, the limitation of the truncated space of photon number also leads to the separation of the numerical and analytical solutions at high pump power for the second-order autocorrelation function $g_s^{(2)}(0)$ [see Fig. S5(f)]. The analytical value is slightly larger than the numerical simulation value at high pump power due to the influence of the high Fock states we neglected. For example, $g_s^{(2)}(0)=1.22$ for the numerical solution and $g_s^{(2)}(0)=1.68$ for the analytical solution at $\xi\sqrt{P}/\kappa_s=20$. In the case of high pump power, the second-order autocorrelation function is already larger than unity, the photon state is no longer a single photon. This is beyond the topic of this paper. Considering the cost and time of calculation, we do not continue to truncate the space of higher photon numbers to get better coincidence between the numerical and analytical solutions.

B. The Purity-Yield Limitation

In conventional HSPSs, there is a limitation between improving the yield and keeping the purity of single photons [12]. Improving the single-photon yield by increasing the pump laser power inevitably results in the decrease of the purity of single photons. We measure this limitation by multiplying the yield Y and purity Π of single photons, and obtain

$$Y*\Pi=\begin{cases}\dfrac{\tanh^2(\xi\sqrt{P}t)\left(1-\tanh^2(\xi\sqrt{P}t)\right)}{\cosh^2(\xi\sqrt{P}t)}, & g_s^{(2)}(0)\leq 1,\\ 0, & g_s^{(2)}(0)>1.\end{cases} \tag{S53}$$

Approximately to the first order, we have $Y*\Pi=(\xi\sqrt{P}t)^2[1-2(\xi\sqrt{P}t)^2]$. For a small $\xi\sqrt{P}t$, we can find that $Y*\Pi$ has a maximum value. This suggests that there is a limitation to the improvement of purity and yield for conventional HSPSs.

In Fig. S6, we show the purity-yield product $Y*\Pi$ of single photons in non-blockade case as a function of the pump laser power $\xi\sqrt{P}$. The analytical and the numerical solutions agree very well. When $\xi\sqrt{P}/\kappa_s>11$, $g_s^{(2)}(0)>1$, thus the value of $Y*\Pi$ is equal to zero. From the Fig. S6, as we expected, the product of the yield and the purity has a maximum value about 0.09 at $\xi\sqrt{P}/\kappa_s=6.4$. Therefore, there is an upper limitation between improving the yield and keeping the purity of single photons in the non-blockade case. Our scheme can break through this purity-yield limitation via photon blockade, which has been discussed in the main text.

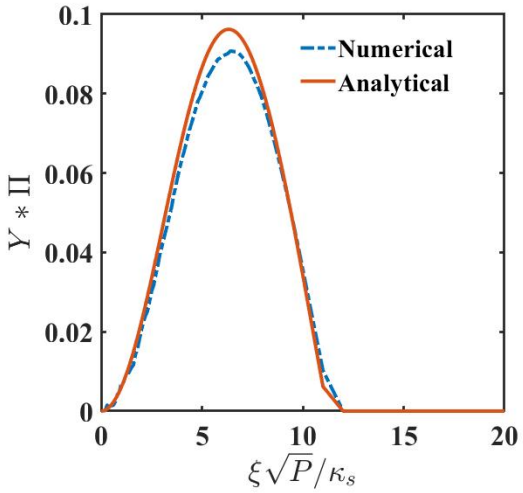

FIG. S6. The product of the yield Y and the purity Π of single photons versus the effective pump power $\xi\sqrt{P}$ without the photon blockade. Here, the duration of pulse has been fixed at $\kappa_s\tau_p=\pi/40$. Other parameters are $\kappa_s=\kappa_i=1$.

IV. THE INFLUENCE OF NON-PAIRED PHOTON STATES

In this section, we discuss the influence of non-paired photon states, i.e., $|n_s,n_i\rangle$ with $n_s\neq n_i$. Theoretically, in SPDC process, the signal and idler modes are always generated in pairs, as can be seen from the Hamiltonian Eq. (S1). However, there is a very small probability that some of the non-photon-pair states can be excited. In Fig. S7(a), we show the population of different non-photon-pair states as a function of the pump power $\xi\sqrt{P}/\kappa_s$ at the PPI strength $\eta/\kappa_s=80$. Similar to the photon-pair states, we can find that the excitation of non-photon-pair states also increase with the increase of pump power. However, the probability of excitation for non-photon-pair states is very small and mainly concentrated on the single-photon state, i.e., p_{n1} or p_{1m}. For example, for p_{01}, its proportion is much less than 3.5% at $\xi\sqrt{P}/\kappa_s=20$. This is because the strong PPI suppress the excitation of multi-photon states.

For the effect of the non-photon-pair states, we are more concerned with the total contribution $\sum_{n\neq m}P_{nm}$, which is shown in Fig. S7(b). We can find that the total non-photon-pair states excitation decreases with the increase of the

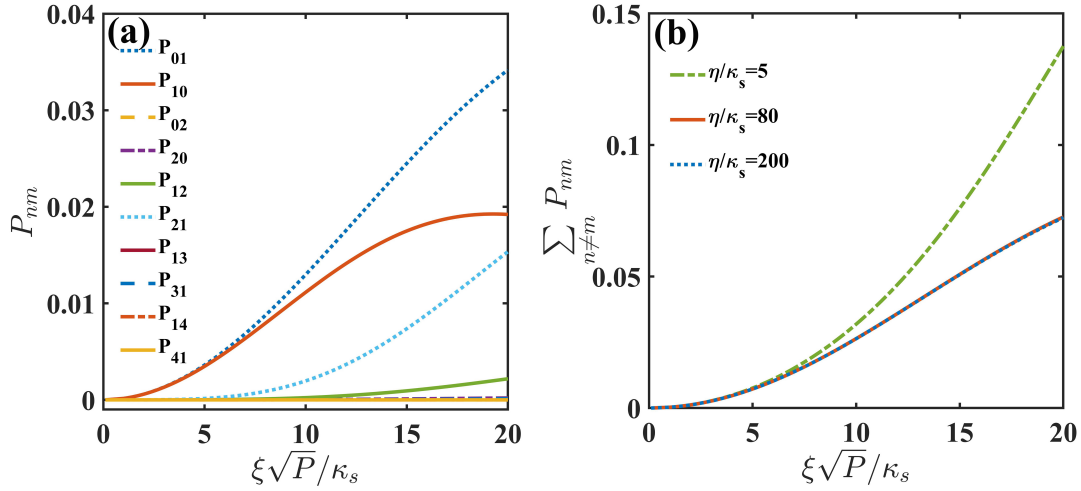

FIG. S7. (a) Population of non-photon-pair states, i.e., $|n_s, n_i\rangle$ $(n_s \neq n_s)$, versus the effective pump power $\xi\sqrt{P}/\kappa_s$. Here we take the PPI strength $\eta/\kappa_s = 80$. (b) The total population contribution of non-photon-pair states as a function of the effective pump power $\xi\sqrt{P}/\kappa_s$ with different PPI strength. The solid red curve and the dashed blue curve completely overlap. Other parameters are $\kappa_s = \kappa_i = 1$ and $\gamma_0 = 0.5\kappa_s$.

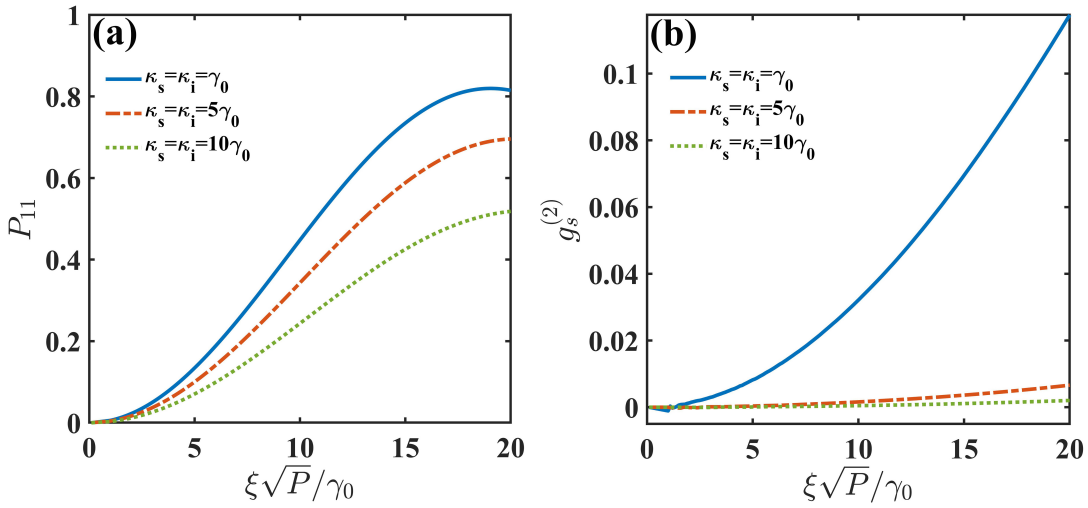

FIG. S8. Population of Fock state $|1,1\rangle$ (a) and the second-order autocorrelation $g_s^{(2)}$ (b) versus the pump power $\xi\sqrt{P}/\gamma_0$ with different decay rates of signal-idler mode. Here, for convenience, we take the decay rate of atoms γ_0 as the scaling rate. Other parameters are $\kappa_s = \kappa_i$ and $\eta/\kappa_s = 80$.

PPI strength, see the dash-dotted green curve for $\eta/\kappa_s = 5$ and the red solid curve for $\eta/\kappa_s = 80$. When $\eta/\kappa_s = 80$, the total contribution of the non-photon-pair states is small, less than about 7% at $\xi\sqrt{P}/\kappa_s = 20$. For a larger PPI strength, since the suppression of multi-photon states is saturated and the contribution of total non-photon-pair states mainly comes from single-photon states, the proportion of total non-photon-pair states remains unchanged, see the dotted blue curve in Fig. S7(b).

In general, in the case of fixed pump pulse duration, the single-photon yield is improved very slowly in the later stage with higher pump power and PPI strength due to the existence of non-photon-pair states. An improved method is the π-pulse excitation mentioned below, which can pump the nonlinear crystal more efficiently to produce the single-photon-pair state.

V. THE INFLUENCE OF THE CAVITY DECAY

Here, we discuss the effect of the decay rate of cavity modes on the yield and purity of single photons in our system. For the sake of simplicity, we study the influence of cavity modes decay rate changes relative to the atomic attenuation rate, that is, take the decay rate of atoms as normalization. At the same time, we assume that the decay rate of the signal mode is equal to that of the idler mode, i.e., $\kappa_s = \kappa_i$.

The Fig. S8(a) and (b) show the population of Fock state $|1,1\rangle$, i.e., P_{11} and the equal time second-order autocorrelation $g_s^{(2)}(0)$ as a function of the pump power $\xi\sqrt{P}/\gamma_0$ with different decay rates of cavity modes, respectively. With the increase of the decay rate of the cavity modes, the yield of single photon decreases, but the purity improves. For example, when $\kappa_s = \kappa_i = \gamma_0$ and $\eta/\kappa_s = 80$, the single-photon yield is 82% and the purity can reach $\sim 90\%$ at $\xi\sqrt{P}/\gamma_0 = 19$, see Fig. S8(a). When the decay rate of cavity modes increases to $5\gamma_0$ and $10\gamma_0$, the yield of single photon decreases to 68% and 51%, respectively, while the purity can increase to 99.4% and 99.9%. We can understand this in terms of multi-photon-pair excitation and decay. When the decay rate of cavity modes increases, the photon-pair states decay to the vacuum state, thus the single-photon yield decreases. Compared with the single-photon-pair state, the multi-photon-pair states decay faster, so the purity of single photon will be improved. In our system, the effect of the cavity modes attenuation can be used as another regulatory parameter to balance the yield and purity of single photons.

VI. π-PULSE EXCITATION

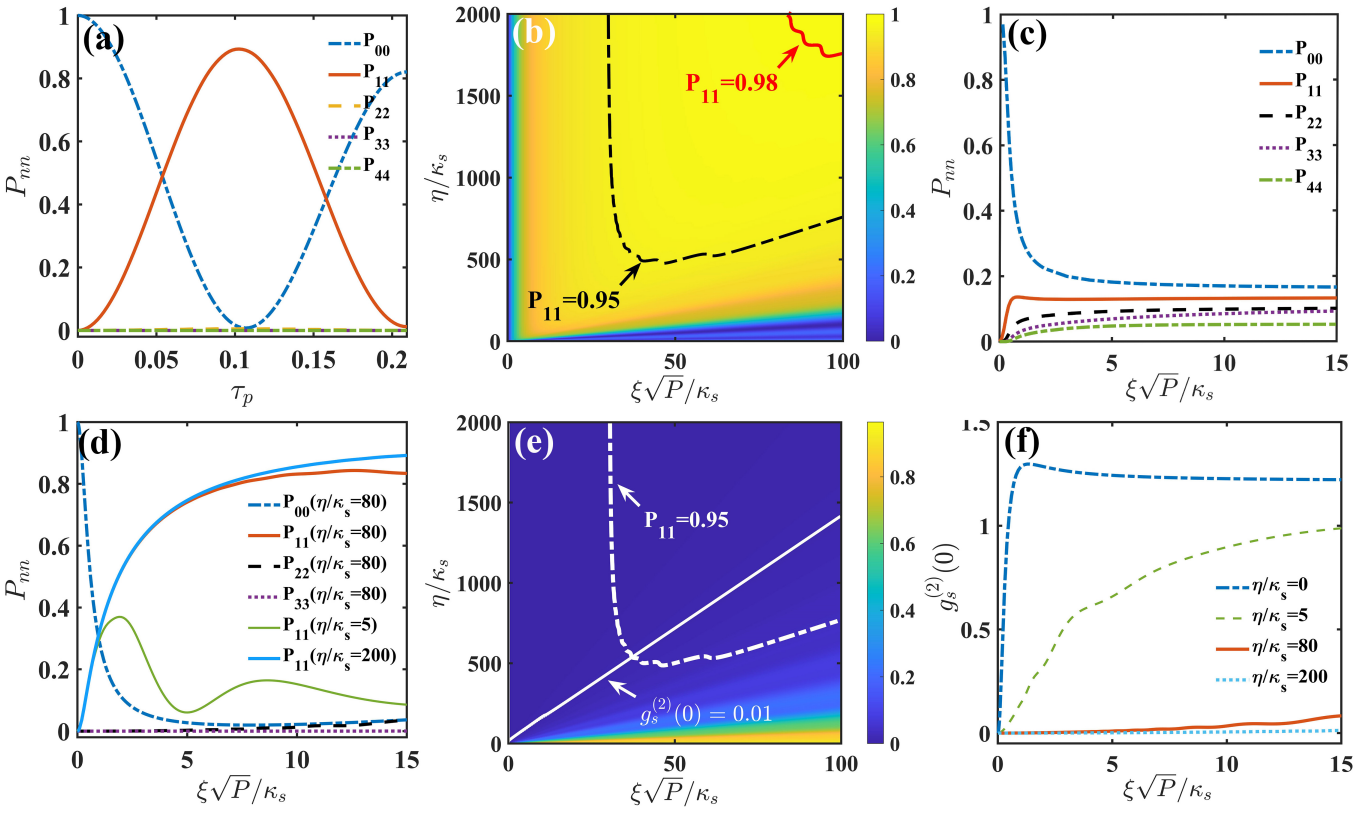

FIG. S9. Population of Fock states $|n_s, n_i\rangle$ and the equal time second-order autocorrelation $g_s^{(2)}(0)$ in π-pulse excitation. (a) The evolution of population of photon-pair states over time. Here $\eta/\kappa_s = 200$ and $\xi\sqrt{P}/\kappa_s = 15$. (b,e) Population of Fock state $|1.1\rangle$, i.e., the probability of single-photon pair P_{11}, and the second-order autocorrelation $g_s^{(2)}$ versus effective pump power $\xi\sqrt{P}$ and the PPI strength η. (c,d,f) Population of Fock states $|n_s, n_i\rangle$ and second-order autocorrelation $g_s^{(2)}$ as a function of effective pump power $\xi\sqrt{P}$, where (c) and (d) correspond to non-blockade and blockade cases, respectively. (f) $g_s^{(2)}$ versus the pump power under different nonlinearities. Other parameters are $\kappa_s = \kappa_i = 1$.

In this section, we discuss the impact of π-pulse excitation in more details. Considering a strong PPI in our system,

high Fock states of photon pairs are suppressed. Therefore, it can be approximately regarded as only vacuum and single-photon pair states in the cavity. Figure S9(a) shows the evolution of the photon pairs of the system over time. It can be found that the time for the system to achieve a complete Rabi-like oscillation between the single-photon pair state $|1,1\rangle$ and the vacuum state is 2π. This proves that our approximation is very valid.

Similar to the main text, we present a two-dimensional diagram of the single-photon pair state excited by the π-pulse excitation with the pump laser power and PPI strength in Fig. S9(b). In the range of $\eta/\kappa_s \geq 500$ and $\xi\sqrt{P}/\kappa_s > 40$, i.e., the black dashed curve, the single-photon yield can be very high, more than 95%. For a larger pump power and PPI strength, the yield can be higher than 98%, see the solid red curve. We can find that π-pulse excitation can further improve the yield of single photon compared to a fixed-duration pump pulse. Note that when the pump power is small, the blockade effect has less influence on the single-photon yield, even if the PPI is strong, as shown on the left side of Fig. S9(b). This is due to the limitation of the excitation of signal photons in the cavity. At low pump power, although the excitation of high Fock states of photon pairs is suppressed, their proportion is very low. On the contrary, at low pump power, the proportion of vacuum states is very high. Therefore the influence of the blockade effect on the yield of single photon is easy to reach saturation. This also happens in the case of fixed pump laser pulse duration, see Fig. 2(a) in the main text.

The dependence of the probabilities of photon pairs on the pump laser power with and without considering the PPI in the case of π-pulse excitation is shown in Fig. S9(c),(d). According to Eq. (S40), the probabilities of different photon-pair states in the absence of photon blockade should be constant. However, we note that these probabilities have a process of increasing form zero when the pump laser power is small, as shown in Fig. S9(c). This is because there is a competition between the pump power and dissipation of the noise photons we considered. As the pump power increases to a certain extent, the effect of photon dissipation can be neglected, thus the probability of each photon-pair states tends to be stable as we calculated. With the photon blockade, the single-photon yield increases faster than the case of a fixed pump laser duration when the pump laser power is small, see Fig. S9(d).

The equal time second-order autocorrelation $g_s^{(2)}(0)$ is shown as a function of the PPI strength and the pump power in Fig. S9(e). We can obtain a high purity, $\Pi > 99\%$, when η is large enough, indicated by the white solid curve. Therefore, the purity of single photon is significantly improved compared with that of the fixed-duration pump pulse. It is worth noting that, since it is π-pulse excitation, i.e., $2\xi\sqrt{P}\tau_p = \pi$, $g_s^{(2)}(0)$ should not change with the pump power according to Eq. (S51). However, the statistic of the photon states shows an anti-bunching situation at a small power, i.e., $g_s^{(2)}(0) < 1$, see the dash-dotted blue curve in Fig. S9(f). This is also due to the fact that we considered the case of noise photons. Once the pump power reaches a certain level, the dissipation of photons can be neglected, and $g_s^{(2)}(0)$ gradually becomes constant. According the Eq. (S51), we can calculate that $g_s^{(2)}(0)$ is 1.68. However, limited by the truncated space of photon number during simulation, our numerical result is 1.22, which is slightly less than the calculated value.

In general, when we consider a π-pulse excitation, the single-photon pair state $|1,1\rangle$ can be completely populated from the vacuum state and reach the maximum value. Therefore, π-pulse can excite the single-photon pair state more efficiently than the case of a fixed pump pulse duration. At the same time, the purity of single photon remains high due to the photon blockade effect.

VII. QUANTUM TRAJECTORY SIMULATION OF THE OUTPUT PHOTONS

According to the cavity quantum electrodynamics theory, photons in the cavity interact with the environment mainly through two channels. One is the internal losses of the cavity, and the photons dissipate into the environment. The other is the external decay of the cavity, in which photons are transmitted out of the cavity through a specific cavity mirror and be detected by the photon detector. The time for photons to decay outside the cavity depends on the external decay rate of the cavity. Quantum trajectory (QT) provides an effective method for describing the statistical state of photons attenuated outside the cavity. Such photon statistical states are very complicated to describe by the master equation (ME) [13]. Before starting to study our system, we first test two simple cases: the outgoing photons initially prepared in an ideal single-mode cavity and an ideal dual-mode cavity. Then we apply QT approach to our system.

A. The outgoing photons from an ideal single-mode cavity

To test the QT approach, we consider a single-mode optical cavity in which the photons can escape through a specific cavity mirror. According to the QT theory, if a photon escapes from the cavity within a time interval δt, the states of the system will undergo a jump. δt must be small enough so that at most one jump can occur within the

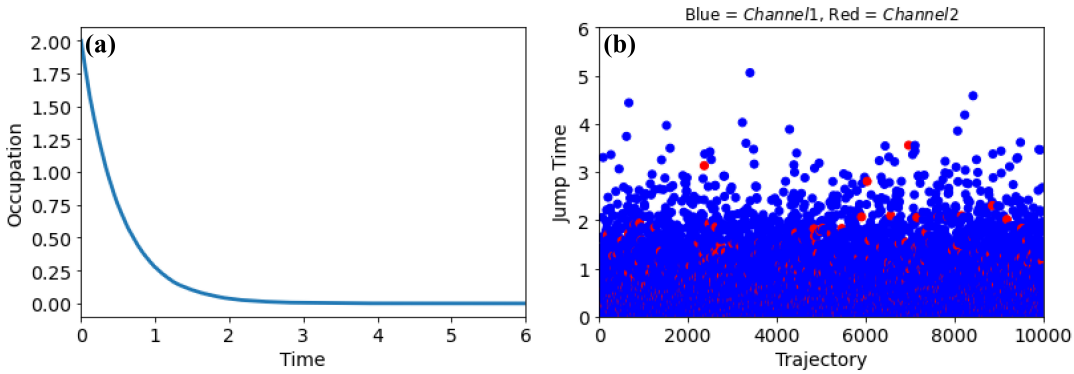

FIG. S10. Simulation of the output photons in a single-mode resonator via QT approach, where the initial state of the cavity is set as $|\psi\rangle = |2\rangle$. (a) The average number of photons in the cavity varies with time after averaging 10000 QTs. (b) Photons escaping from the cavity through different channels, where the blue dots, i.e., the channel 1, are for the external decay channels and the red dots are for the internal decay channels.

time interval δt, that is, at most only one photon is emitted. We assume that there is a photon detector outside the cavity that has the ability to tell whether or not a photon has been emitted. Therefore, in each QT simulation, the number of jumps of the system state corresponds to the number of photons detected by the out-of-cavity detector [14].

We first use the QT approach to study the relationship between the number of photons decayed in each channel and the decay rates. We assume that the initial state of the cavity is $|\psi\rangle = |2\rangle$ and the internal decay rate of the cavity is $\kappa_{in} = 0.044$ and the external decay rate is $\kappa_{ex} = 0.956$, which is consistent with the experimental implementation part in the main text. Using the open-source package QuTip [15], we performed 10000 simulations of the QTs of photons in the cavity. The average results show the change in the number of photons in the cavity over time [see Fig. S10(a)]. Fig. S10(b) visualizes the jumps of photonic states through different channels in each QT simulation. The small blue circles indicate that photons enter the photon detector through the external decay of the cavity, and the small red circles indicate that photons are dissipated into the environment through the internal losses of the cavity. The results show that under 10000 QTs, the proportion of photons entering the photon detector through the external decay channel of the cavity is 95.595%, and the proportion of photons attenuated internally is 4.405%. Therefore, the probability of photons escaped from the cavity is proportional to the external decay ratio of the cavity. The escape efficiency can be defined as

$$\eta_{esp} = \frac{\kappa_{ex}}{\kappa_{ex} + \kappa_{in}}, \tag{S54}$$

where, κ_{ex} and κ_{in} correspond to the external and internal losses of the cavity, respectively. Below, we assume that the photons in the cavity have a perfect escape efficiency, that is, the internal losses of the cavity is neglected (the issue of escape efficiency is discussed in the main text).

Then we investigated the statistical properties of the output photons. We assume that the initial state of the single-mode resonator is $|\psi\rangle = (|0\rangle + |1\rangle + |2\rangle)/\sqrt{3}$, where the numbers in ket correspond to the $n-$photon Fock state. We take the external decay rate of the cavity $\kappa = \kappa_{ex}$ as a normalization. From the Fig. S11(d), we can find that in the period of $\kappa t = 6$, the photons in the cavity are completely emitted. For a single QT, if the photon states in the cavity do not jump , it means that the detector will not detect the photons, which correspond to the situation in Fig. S11(a); if the detector detects a photon, it means that the photon states in the cavity have occurred one jump, corresponding to Fig. S11(b); if two photons are detected, the photon states in the cavity has two jumps, which corresponds to Fig. S11(c).

When we make 10000 similar QTs and count the number of jumps in each QT, we can determine the statistical properties of the photons detected by the photon detector, that is, the statistical properties of the output photons state. The results show that, after 10000 simulations, the probability of detecting one photon is 33.64%, two photons is 33.18% and no photon is 33.18% in the time period of $\kappa t = 6$. Taking into account the limitation of the number of QT simulations, the statistical properties of photons detected by the detector in the $\kappa t = 6$ period are consistent with the initial photon state statistics in the cavity.

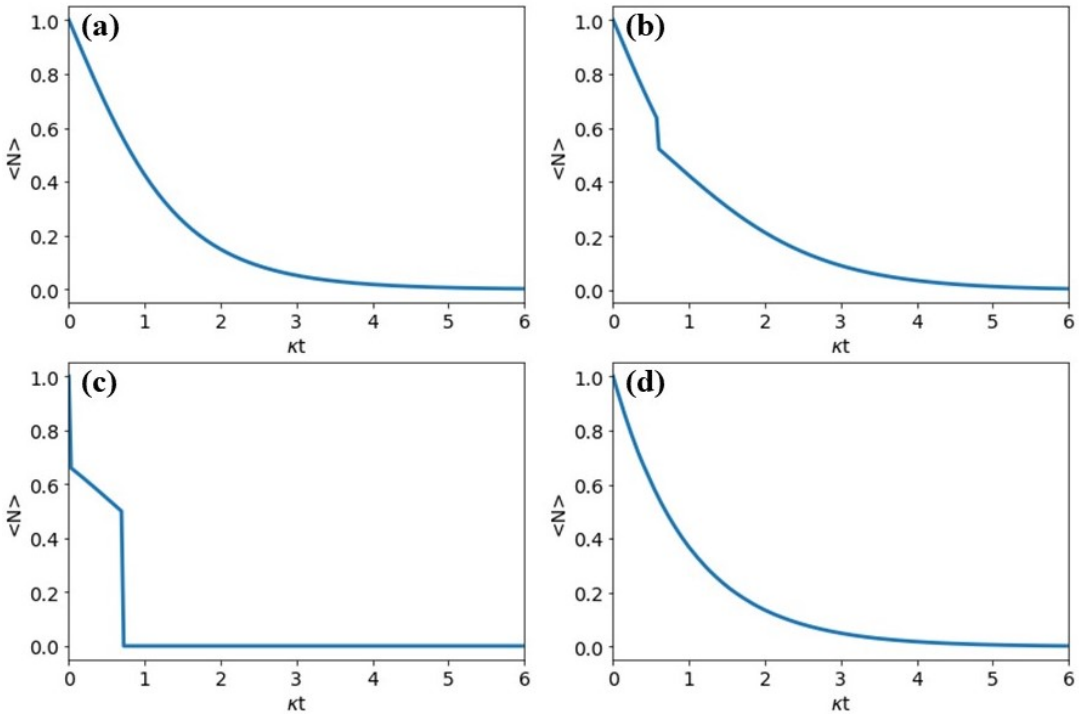

FIG. S11. Simulation of the output photons in a single-mode resonator, where the horizontal coordinate represents the photonic decay time in the cavity and the ordinate represents the average number of photons in the cavity. (a),(b) and (c) correspond to a single QT result with zero, one and two quantum jumps, respectively; (d), averages of 10000 similar QTs.

B. The outgoing photons from an ideal dual-mode cavity

To test the validity of the QT approach in a dual-mode cavity, we consider the case of the dual-mode resonator and assume that both two modes have the same decay rate κ. We assume that the initial state of the dual-mode resonator is $|\psi\rangle = (|0_s 0_i\rangle + |1_s 1_i\rangle + |2_s 2_i\rangle)/\sqrt{3}$, where the subscripts represent the two resonant modes of signal and idler photons respectively. The results are shown in Fig. S12. As can be seen from the Fig. S12(a), the signal and idler photons completely decay out from the cavity in the attenuation time period of $\kappa t = 6$. Since the initial signal and idler photons are paired, their decay curves overlap. Fig. S12(b) visualizes the jump of photonic states in the cavity after running 10000 QT simulations, where the small blue circles represent the jumps of signal photons, i.e., the cavity emits a signal photon, while the small red circles indicate the idler photon jumps and the cavity emits an idler photon. We assume that the detector can distinguish between signal and idler photons. For each QT simulation, if both the intra-cavity signal and idler photons have one jump, the detector can detect a single-photon pair during the decay time period; if the signal and idler photons jump twice, the detector can detect a two-photon pair; if there is no jump, the photons won't be detected by the detector.

Similar to single-mode cavity calculation, for 10000 QT simulations, the statistical properties of the output photons can be obtained by counting the number of photon jumps in the cavity. The results show that, after 10000 simulations, the probability of detecting single-photon pair is 33.11% in the decay time period of $\kappa t = 6$, two-photon pair is 33.69%, and zero-photon is 33.20%. The statistics of the output photons are consistent with those of the initial photons in the cavity. This is reasonable because we have neglected the internal losses of the cavity.

C. The output photons from our cavity-enhanced SPDC system

Now we return to the system discussed in our main text, we use the QT approach to simulate the output photons. Figure S13 shows the population of single-photon pair in the cavity varies with different pump powers when the pump laser is switched off. It can be found that the results of the ME are consistent with the QT approach for both the fixed-duration pulse excitation and π-pulse excitation.

We set the whole detection period of the detectors to $\kappa_s t = 6$. This period is long enough so that the single photon

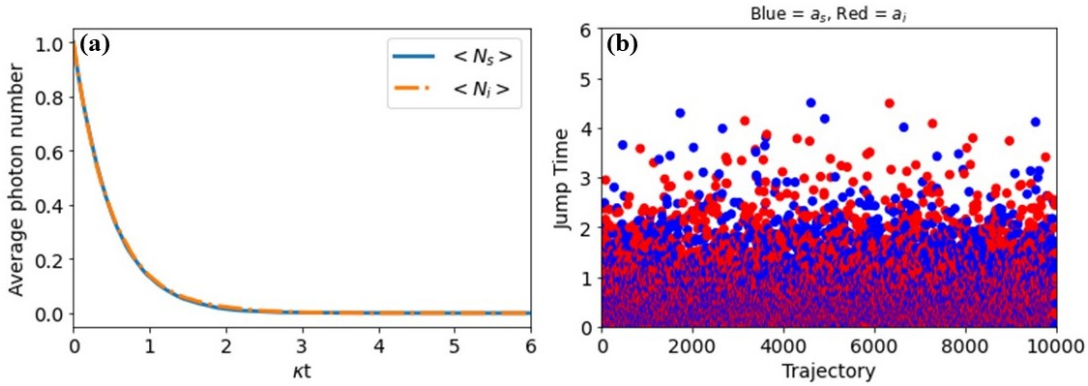

FIG. S12. Simulation of the output photons in a dual-mode resonator via QT approach. (a) The average photon number in the cavity varies with the decay time, in which the solid blue and the dotted yellow curves represent the signal and idler photons respectively. (b) showing which times and operators (blue for signal photons and red for idler photons) are responsible for the jump of states in the cavity in 10000 QT simulations

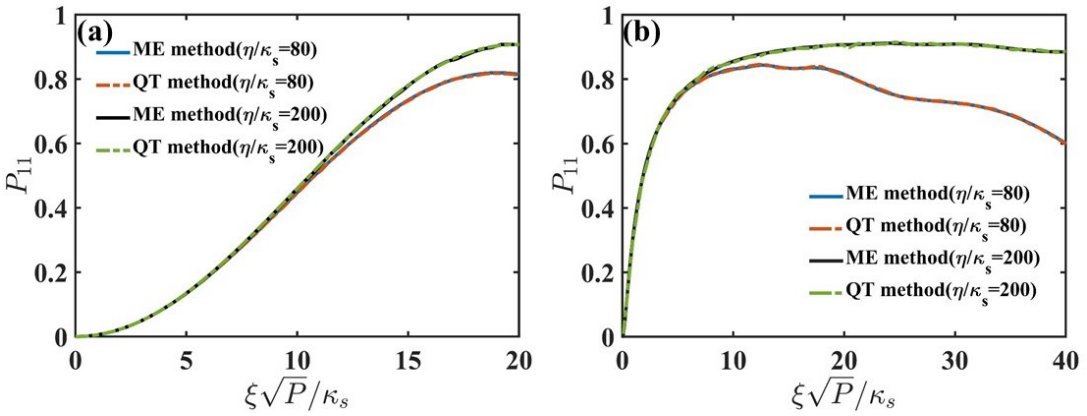

FIG. S13. Population of Fock states $|1,1\rangle$, i.e., the probability of single-photon pair, versus the pump laser power $\xi\sqrt{P}$, where the solid curves are calculated by the ME method, and the dashed curves are calculated by the QT method. (a) is for the case with a fixed duration $\kappa_s\tau_p = \pi/40$, (b) is for the case with $\pi-$pulse excitation.

generated in the cavity can completely escape and can also separate from the subsequent photon pulse. The pump and control pulses are shown in Fig. S14(a). When the pump and control pulses are switched off, the photons prepared in the cavity decay out through the cavity mirror $M2$ and is measured by the detector. In real operation, the control laser can be constantly applied to Rb atoms to avoid temporal synchronization of pulses. We choose the pump pulse with fixed duration $\kappa_s\tau_p = \pi/40$ as an example, and take the pump power $\xi\sqrt{P}/\kappa_s = 18$. It can be found that the signal photons and the idler photons in the cavity completely escaped from the cavity within $\kappa_s t = 6$ [see Fig. S14(b) for $\eta/\kappa_s = 80$ and Fig. S14(c) for $\eta/\kappa_s = 200$]. Since the duration of the pump pulse is very small compared to the time period of decay, the probability of photon escaping during the pumping stage is negligible. This can be seen from the simulation results that the probability of n-photon pairs measured by the detectors is in consistence with that in the cavity. The results of the QT simulations are shown in the main text, see Fig. 2(b), Fig. 3(b) and Fig. 4.

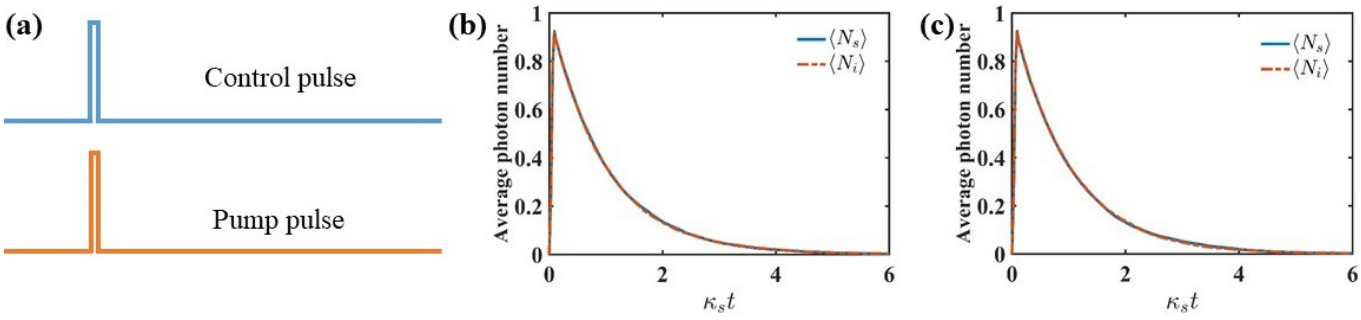

FIG. S14. QT simulation of our cavity-enhanced HSPS for $\eta/\kappa_s = 80$ and $\eta/\kappa_s = 200$. (a) Control pulse and pump pulse settings. (b) The average number of photons in the cavity varies with time. It can be seen that the photons completely escape from the cavity at the time period of $\kappa_s t = 6$.

[1] Nicolas Sangouard, Christoph Simon, Hugues de Riedmatten, and Nicolas Gisin, "Quantum repeaters based on atomic ensembles and linear optics," Rev. Mod. Phys. **83**, 33–80 (2011).

[2] Marlan O. Scully and M. Suhail Zubairy, Quantum Optics (Cambridge University Press, 1997).

[3] Katsunari Okamoto, Fundamentals of Optical Waveguides (Academic press, 2006).

[4] Jiteng Sheng, Xihua Yang, Haibin Wu, and Min Xiao, "Modified self-kerr-nonlinearity in a four-level N-type atomic system," Phys. Rev. A **84**, 053820 (2011).

[5] Jiangshan Tang, Yang Wu, Zhenkai Wang, Hui Sun, Lei Tang, Han Zhang, Tao Li, Yanqin Lu, Min Xiao, and Keyu Xia, "Vacuum-induced surface-acoustic-wave phonon blockade," Phys. Rev. A **101**, 053802 (2020).

[6] Sylvain Fasel, Olivier Alibart, Sébastien Tanzilli, Pascal Baldi, Alexios Beveratos, Nicolas Gisin, and Hugo Zbinden, "High-quality asynchronous heralded single-photon source at telecom wavelength," New J. Phys. **6**, 163–163 (2004).

[7] Matthias Scholz, Lars Koch, and Oliver Benson, "Statistics of narrow-band single photons for quantum memories generated by ultrabright cavity-enhanced parametric down-conversion," Phys. Rev. Lett. **102**, 063603 (2009).

[8] E. Bocquillon, C. Couteau, M. Razavi, R. Laflamme, and G. Weihs, "Coherence measures for heralded single-photon sources," Phys. Rev. A **79**, 035801 (2009).

[9] Kevin A Fischer, Lukas Hanschke, Jakob Wierzbowski, Tobias Simmet, Constantin Dory, Jonathan J Finley, Jelena Vučković, and Kai Müller, "Signatures of two-photon pulses from a quantum two-level system," Nat. Phys. **13**, 649–654 (2017).

[10] Xing Ding, Yu He, Z. C. Duan, Niels Gregersen, M. C. Chen, S. Unsleber, S. Maier, Christian Schneider, Martin Kamp, Sven Höfling, Chao-Yang Lu, and Jian-Wei Pan, "On-demand single photons with high extraction efficiency and near-unity indistinguishability from a resonantly driven quantum dot in a micropillar," Phys. Rev. Lett. **116**, 020401 (2016).

[11] Pascale Senellart, Glenn Solomon, and Andrew White, "High-performance semiconductor quantum-dot single-photon sources," Nat. Nanotechnol. **12**, 1026–1039 (2017).

[12] Andreas Christ and Christine Silberhorn, "Limits on the deterministic creation of pure single-photon states using parametric down-conversion," Phys. Rev. A **85**, 023829 (2012).

[13] M. B. Plenio and P. L. Knight, "The quantum-jump approach to dissipative dynamics in quantum optics," Rev. Mod. Phys. **70**, 101–144 (1998).

[14] Sébastien Gleyzes, Stefan Kuhr, Christine Guerlin, Julien Bernu, Samuel Deléglise, Ulrich Busk Hoff, Michel Brune, Jean-Michel Raimond, and Serge Haroche, "Quantum jumps of light recording the birth and death of a photon in a cavity," Nature (London) **446**, 297–300 (2007).

[15] J. R. Johansson, P. D. Nation, and Franco Nori, "Qutip: an open-source python framework for the dynamics of open quantum systems," Comput. Phys. Commun. **183**, 1760–1772 (2012).